










The demographics of obscured AGN from X-ray spectroscopy guided by multiwavelength information

Brivael Laloux ^{1,2★}, Antonis Georgakakis ^{1★}, Carolina Andonie ², David M. Alexander,²
 Angel Ruiz ¹, David J. Rosario,^{2,3} James Aird ^{4,5}, Johannes Buchner ⁶, Francisco J. Carrera,⁷
 Andrea Lapi,⁸ Cristina Ramos Almeida ^{9,10}, Mara Salvato ^{6,11} and Francesco Shankar ¹²

¹*Institute for Astronomy & Astrophysics, National Observatory of Athens, V. Paulou & I. Metaxa, 11532, Greece*

²*Centre for Extragalactic Astronomy, Department of Physics, Durham University, Durham, DH1 3LE, UK*

³*School of Mathematics, Statistics and Physics, Newcastle University, Newcastle upon Tyne, NE1 7RU, UK*

⁴*Institute for astronomy, University of Edinburgh, Royal observatory, Edinburgh EH9 3HJ, UK*

⁵*School of Physics & Astronomy, University of Leicester, University Road, Leicester LE1 7RJ, UK*

⁶*Max Planck Institute for Extraterrestrial Physics, Giessenbachstrasse, D-85741 Garching, Germany*

⁷*Instituto de Física de Cantabria (CSIC – Universidad de Cantabria), Avenida de los Castros, E-39005 Santander, Spain*

⁸*SISSA, Via Bonomea 265, I-34136 Trieste, Italy*

⁹*Instituto de Astrofísica de Canarias, Calle Vía Láctea, s/n, La Laguna, E-38205 Tenerife, Spain*

¹⁰*Departamento de Astrofísica, Universidad de La Laguna, La Laguna, E-38206 Tenerife, Spain*

¹¹*Exzellenzcluster ORIGINS, Boltzmannstr. 2, D-85748 Garching, Germany*

¹²*Department of Physics and Astronomy, University of Southampton, Highfield SO17 1BJ, UK*

Accepted 2022 November 4. Received 2022 October 18; in original form 2022 September 2

ABSTRACT

A complete census of active galactic nuclei (AGNs) is a prerequisite for understanding the growth of supermassive black holes across cosmic time. A significant challenge towards this goal is the whereabouts of heavily obscured AGN that remain uncertain. This paper sets new constraints on the demographics of this population by developing a methodology that combines X-ray spectral information with priors derived from multiwavelength observations. We select X-ray AGN in the *Chandra* COSMOS Legacy survey and fit their 2.2–500 μm spectral energy distributions with galaxy and AGN templates to determine the mid-infrared (6 μm) luminosity of the AGN component. Empirical correlations between X-ray and 6 μm luminosities are then adopted to infer the intrinsic accretion luminosity at X-rays for individual AGN. This is used as prior information in our Bayesian X-ray spectral analysis to estimate physical properties, such as line-of-sight obscuration. Our approach breaks the degeneracies between accretion luminosity and obscuration that affect X-ray spectral analysis, particularly for the most heavily obscured (Compton-Thick) AGN with low photon counts X-ray spectra. The X-ray spectral results are then combined with the selection function of the *Chandra* COSMOS Legacy survey to derive the AGN space density and a Compton-Thick fraction of $21.0_{-9.9}^{+16.1}$ per cent at redshifts $z < 0.5$. At higher redshift, our analysis suggests upper limits to the Compton-Thick AGN fraction of $\lesssim 40$ per cent. These estimates are at the low end of the range of values determined in the literature and underline the importance of multiwavelength approaches for tackling the challenge of heavily obscured AGN demographics.

Key words: galaxies: active – X-rays: general – quasars: general – infrared: galaxies.

1 INTRODUCTION

Supermassive black holes (SMBHs) are found to be ubiquitous in the nuclear regions of local galaxies (Kormendy & Ho 2013). These compact objects are thought to grow their masses either via accretion of material from their surroundings (e.g. Soltan 1982; Alexander & Hickox 2012) or through merging with other black holes (e.g. Volonteri, Haardt & Madau 2003; O’Neill et al. 2022). During such active periods, large amounts of energy can be produced and observed as electromagnetic radiation at different parts of the

spectrum. The class of astrophysical sources that correspond to such events are broadly dubbed active galactic nuclei (AGNs; Antonucci 1993; Urry & Padovani 1995; Padovani et al. 2017). Observational measurements of the space density of AGN in the Universe as a function of cosmic time provide essential constraints on the growth history of SMBHs we observe in the local Universe (Marconi et al. 2004). Although simple in principle, counting AGN in a cosmological volume is challenging because of both observational limitations and the phenomenological complexity of active black holes. For example, the amount of energy radiated by individual accretion events brackets many orders of magnitude and strongly depends on wavelength. Therefore, accounting for lower luminosity events in flux-limited samples is not straightforward and requires

* E-mail: brivael.laloux@noa.gr (BL); age@noa.gr (AG)

a good understanding of observational biases and selection effects. Moreover, a substantial fraction of SMBHs in the Universe is believed to grow their masses behind clouds of dust and gas (Maiolino et al. 1998; Risaliti, Maiolino & Salvati 1999) that attenuate the emitted radiation and render the identification of such systems difficult. This introduces biases in AGN counting experiments and can lead to a significant underestimation of the true size of the underlying population. Accounting for this effect requires a handle on the obscuration distribution of AGN. This has motivated observational programmes that aim to constrain the fraction of obscured AGN in the Universe and provide an unbiased census of the active SMBH population (e.g. Hickox & Alexander 2018).

Among the different wavebands available for studying AGN obscuration, the X-ray regime offers several advantages. X-ray photons, particularly at harder rest-frame energies ($\gtrsim 2$ keV), are less affected by intervening gas clouds compared to e.g. UV/optical, and can, therefore, provide the least biased samples for demographical investigations. Besides, at these energies, the contamination of the host galaxy by X-ray binaries or supernova remnants is low. Moreover, any obscuring material along the line of sight (LOS) imprints characteristic signatures on the X-ray spectra of AGN. This, in turn, translates into direct measurements of the density of the intervening obscuring clouds for individual AGN since X-ray imaging observations typically also provide spectral information. Having a handle on the level of obscuration means the possibility to quantify the selection function of X-ray surveys, i.e. the probability of detecting AGN of a given intrinsic luminosity, redshift and obscuration. This key feature enables the crucial step from an observational census of AGN (i.e. a sample) to the demographics of the underlying population. As a result, the most detailed description of the whereabouts of obscured AGN to date has been painted by high-energy survey programmes (e.g. Barger et al. 2003; Ueda et al. 2003; Della Ceca et al. 2008; Ueda et al. 2014; Burlon et al. 2011; Alexander et al. 2013; Aird et al. 2015; Buchner et al. 2015).

X-ray surveys have also identified a deeply buried AGN population, for which the surrounding obscuring material is optically thick even to X-ray photons (e.g. Ricci et al. 2015). The LOS obscuration of these sources, parametrized by the neutral hydrogen column density, N_{H} , exceeds the Thomson scattering limit, $N_{\text{H}} > 1.5 \times 10^{24} \text{ cm}^{-2}$. These sources are often referred to as Compton-Thick (CTK). Conversely, sources with a lower column density are referred to as Compton-Thin (CTN). The direct X-ray emission of CTK sources is largely suppressed by both photoelectric absorption and Compton scattering. Their X-ray spectra are thought to be dominated by indirect radiation, i.e. photons that have been scattered off obscuring material into the LOS. This produces a characteristic spectral shape that includes a flat continuum with superimposed strong emission lines, the most prominent of which is the Fe K α at 6.4 keV (e.g. Levenson et al. 2006; Nandra et al. 2007), and an excess of high energy photons (> 10 keV) forming the so-called Compton hump (Piro, Yamauchi & Matsuoka 1990). However, because of the high level of obscuration, CTK AGN appear X-ray faint and are typically detected at the flux limits of current extragalactic X-ray surveys. As a result, their spectra typically suffer from low count statistics, which translates into significant uncertainties in the determination of their intrinsic properties, such as accretion luminosity and column density (Buchner et al. 2015; Saha, Markowitz & Buchner 2022). Additional information on these sources comes from the shape and normalization of the Cosmic diffuse X-ray Background (CXB) spectrum, which is dominated by the integrated emission of all AGN throughout the Universe. The reconstruction of the CXB using AGN population synthesis models points to a potentially significant

population of CTK sources, larger than the observed one (Gilli, Comastri & Hasinger 2007; Akylas et al. 2012; Ananna et al. 2019). Nevertheless, the exact space density of this population depends on the modelling details such as the shape of the intrinsic spectrum of individual AGN (Akylas et al. 2016).

The InfraRed (IR) part of the electromagnetic spectrum provides an alternative wavelength regime for studying heavily obscured AGN. Indeed, UV/optical photons emitted by the accretion disc are absorbed by circumnuclear dust that re-emits the energy in the IR band. Therefore, the reprocessed radiation field of the active black hole appears as thermal radiation in the (mid-)IR part of the electromagnetic spectrum. Heavily obscured AGN missed by X-ray observations should in principle be present in (mid-)IR surveys, as it is the obscuring material itself that emits reprocessed radiation. The main limitation in finding them is that dust clouds heated by star formation events also emit copious amounts of energy in the IR wavelength regime. This component can dominate the thermal emission of AGN, making their identification difficult. The contrast between star formation and AGN thermal radiation is larger in the mid-IR because of the different temperatures of the medium heated by each process. It is, therefore, easier to isolate the AGN component in the mid-IR and separate it from stellar processes in the host galaxy. This has led to studies that use the shape of the mid-IR continuum (e.g. Park et al. 2010), mid-IR colour diagnostics (e.g. Donley et al. 2012; Messias et al. 2012; Mateos et al. 2012; Stern 2015; Assef et al. 2018) or template fits to multiwavelength (ultra-violet to IR) photometric observations (e.g. Pouliaxis et al. 2020; Mountrichas et al. 2021; Thorne et al. 2022) to compile AGN samples. These can be combined with X-ray observations to search for signatures of high levels LOS obscuration that blocks the direct view to the central engine at X-rays (e.g. Stern et al. 2014; Del Moro et al. 2016; Hickox & Alexander 2018; Vito et al. 2018). The key feature of the mid-IR observations in this type of analysis is that they are thought to provide a good proxy of the intrinsic accretion luminosity even in the case of deeply buried AGN (e.g. Risaliti et al. 1999; Gandhi et al. 2009). Sources that appear X-ray faint for their mid-IR luminosity are obscured AGN candidates (Georgantopoulos et al. 2011). This type of analysis suggests the presence of heavily obscured AGN in the mid-IR that are likely underrepresented in X-ray surveys. However, the selection function of mid-IR AGN samples is often complex and depends on the contrast between the accretion luminosity and the stellar emission of the host galaxy. As a result, the calculation of the space density of the underlying population from mid-IR selected samples is not straightforward (but see Delvecchio et al. 2014; Assef et al. 2015).

This work presents a methodology that combines X-ray and mid-IR information within a Bayesian framework to constrain the space density of heavily obscured AGN. At the core of the method are X-ray observations that provide estimates of the column density N_{H} of individual sources and a well-understood sample selection function. IR photometry is coupled with template fits to yield estimates of the reprocessed accretion luminosity and help improve X-ray spectral constraints. Section 2 describes the multiwavelength observations used in the analysis. Section 3 describes the extraction and fitting of the X-ray spectra and compares the inferred X-ray spectral parameters with previous studies. Section 4 presents the new methodology to improve the X-ray fitting by combining it with AGN mid-IR prior information. In Section 5, the X-ray spectral analysis results are used to infer the obscured AGN demographics and constrain the AGN space density and intrinsic CTK fraction as a function of z , L_{X} , and N_{H} . We discuss our results in Section 6, and summarize our conclusions in Section 7. This paper adopts a

cosmology with a Hubble constant of $H_0 = 70 \text{ km s}^{-1} \text{ Mpc}^{-1}$, mass density parameter, $\Omega_M = 0.3$. and effective mass density of the dark matter $\Omega_\Lambda = 0.7$.

2 DATA

This paper uses data from the Cosmic Evolution Survey (COSMOS) field (Scoville et al. 2007a), which benefits from a large number of multiwavelength observations over an area of nearly 2 deg^2 . Of particular interest to this work are the *Chandra* X-ray survey of this field (Civano et al. 2016) that is used to select AGN, and the multiwavelength photometry catalogue presented by Jin et al. (2018). The latter is used to perform spectral energy distribution (SED) templates fitting of the X-ray sources in our sample and provide independent constraints on their accretion luminosities. The various data sets used in our analysis are described below.

2.1 *Chandra* COSMOS Legacy X-ray survey

We use X-ray data obtained as part of the *Chandra* COSMOS (Elvis et al. 2009) and *Chandra* COSMOS Legacy (Civano et al. 2016) survey programmes. The former consists of 36 overlapping pointings observed by the *Chandra*/ACIS-I detector. The latter programme provides an additional 56 *Chandra*/ACIS-I pointings. The two programmes together cover a total area of about 2 deg^2 with a homogeneous exposure time of about 160 ks for the inner 1.5 deg^2 and 80 ks for the outer regions. The flux limit of the survey in the 0.5–10 keV band is $8.9 \times 10^{-16} \text{ erg s}^{-1}$. These observations are reduced using the analysis and source detection pipeline described by Laird et al. (2009) and Nandra et al. (2015). Sources are detected independently in four spectral bands 0.5–2 keV (soft), 2–7 keV (hard), 4–7 keV (ultra-hard), and 0.5–7 keV (full). The wavelet-based source detection algorithm implemented in the WAVDETECT task of the CIAO (*Chandra* Interactive Analysis of Observations) data analysis system (Fruscione et al. 2006) is used to provide a preliminary seed source list in each of the bands above. Photons are then extracted at the positions of these sources within apertures of variable size that correspond to the 70 per cent encircled energy fraction (EEF) radius of the *Chandra* point spread function (PSF). The background expectation value in each aperture and spectral band is also estimated after removing the contribution of source photons from the corresponding images. The extracted photons and background values at the source positions are then used to calculate the Poisson false detection probability that the observed number of photons results only from background fluctuations. A source is qualified as such if the Poisson false detection probability is $< 4 \times 10^{-6}$ (4.5σ). There are overall 3627 X-ray sources detected in the $\sim 2 \text{ deg}^2$ area of the *Chandra* COSMOS Legacy survey field. Of these sources, 3372, 2772, 2140, and 971 are detected in the full, soft, hard, and ultra-hard bands, respectively, as indicated in the last row of Table 1. This catalogue has already been presented in Georgakakis et al. (2017) and has been used in Aird, Coil & Georgakakis (2017, 2018, 2019). One of the motivations of our analysis is the demographics of heavily obscured AGN, and therefore, the hard band sample with 2140 X-ray sources is of particular interest.

Also important for our analysis is the selection function of the X-ray sample, i.e. the probability of detecting within the *Chandra* COSMOS Legacy survey an X-ray AGN with a given set of intrinsic properties (e.g. accretion luminosity, LOS obscuration, redshift). For that purpose, we use sensitivity maps generated using the methodology described in Georgakakis et al. (2008) and quantify the detection probability of an X-ray source with a specific photon

Table 1. Number of sources in the *Chandra* COSMOS Legacy detected in different energy bands, full (0.5–7 keV), soft (0.5–2 keV), hard (2–7 keV), ultra-hard (4–7 keV), and any of these bands. The number of sources with spectroscopic, photometric, or no redshift measurement is also shown for each subsample. The parenthesis below indicates the number of sources for each band and redshift category after applying the spatial overlap mask (see Section 2.2).

Bands	Full 0.5–7 keV	Soft 0.5–2 keV	Hard 2–7 keV	Ultra-hard 4–7 keV	Any Band
z spectro	1825 (1469)	1562 (1250)	1318 (1071)	726 (573)	1917 (1551)
z photo	1405 (1146)	1061 (864)	773 (629)	227 (184)	1527 (1259)
No z	142 (119)	149 (122)	49 (44)	18 (17)	183 (155)
Total	3372 (2734)	2772 (2236)	2140 (1744)	971 (774)	3627 (2965)

count rate as a function of its position within the surveyed area. In later sections, we combine these sensitivity maps with AGN X-ray spectral models to link the probability of detection to the AGN intrinsic properties.

The X-ray sources are matched with their optical counterparts using different catalogues, including S-COSMOS (Sanders et al. 2007) and the COSMOS Intermediate and Broad Band Photometry Catalogue 2008 (Capak et al. 2007). The identification is performed using the likelihood ratio method (Sutherland & Saunders 1992; Brusa et al. 2007) which takes into account the separation between the X-ray and optical position, but also the counterpart magnitude with respect to the background magnitude distribution as a prior. More details on the identification methodology applied to the COSMOS Legacy field can be found in Aird et al. (2015).

The compilation of spectroscopic and photometric redshifts for our X-ray sources is presented in Georgakakis et al. (2017). The photometric redshift estimates are primarily from Marchesi et al. (2016a) based on methods presented by Salvato et al. (2011). For the X-ray sources in our data reduction that do not appear in the Marchesi et al. (2016a) catalogue, photometric redshifts are estimated following the methods described in Aird et al. (2015). Among the 3627 X-ray sources, 1917 have a spectroscopic redshift, 1527 of the remaining have a photometric redshift, and 183 do not have any redshift estimation. Table 1 presents the number of sources detected in each X-ray band as a function of the redshift type (e.g. photometric versus spectroscopic).

2.2 COSMOS multiwavelength catalogue

We use the ‘super-deblended’ far-IR to (sub)millimetre photometric catalogue of the COSMOS field presented by Jin et al. (2018). They selected samples of galaxies detected at $2.2 \mu\text{m}$, $24 \mu\text{m}$ and radio frequencies (3 GHz) as priors for de-blending far-IR to sub-mm images from different instruments. They collect IR photometric information from UltraVISTA-DR2 with the k band at $2.2 \mu\text{m}$ (McCracken et al. 2012), Spitzer IRAC at 3.6, 4.5, 5.8, and $8 \mu\text{m}$ (Scoville et al. 2007b), Spitzer MIPS at $24 \mu\text{m}$ (Le Floch et al. 2009), *Herschel* PACS at 100 and $160 \mu\text{m}$ (Lutz et al. 2011), and *Herschel* SPIRE at 250, 350, and $500 \mu\text{m}$ (Griffin et al. 2010). The IR photometry of the Jin et al. (2018) catalogue is used to fit templates of AGN and galaxies and get a measurement of the accretion luminosity (if any) emerging in the IR part of the electromagnetic spectrum. This

information is used in later sections to guide X-ray spectral fits of obscured AGN.

The spatial overlap of the Jin et al. (2018) catalogue and the *Chandra* survey of the COSMOS field is not perfect. We use the Hierarchical Equal Area isoLatitude Pixelization (HEALPix; Górski et al. 2005) tessellation of the sky to determine the Multi-Order-Coverage (MOC; Fernique et al. 2019) maps that define the irregular areas covered by two samples and assess their overlap. The maximum HEALPix order parameter for determining the MOCs is set to 14. This value corresponds to a maximum spatial resolution of about 13 arcsec for the resulting MOCs. It is then straightforward to define the overlap region of the two MOCs and determine which X-ray sources have sky coordinates within the common area of the two samples. This reduces our sample to a total of 2965 X-ray sources, of which 2753, 2282, 1816, and 831 are detected in the full, soft, hard, and ultra-hard bands, respectively.

3 X-RAY SPECTRAL ANALYSIS

In this section, we describe our X-ray-fitting pipeline. We start by extracting the X-ray spectra while optimizing for the signal-to-noise ratio (SNR; Section 3.1). Then, we present the fitting algorithm (Section 3.2) and the adopted X-ray AGN model (Section 3.3). Lastly, we justify our choice of baseline model between different set-ups (Section 3.4) and compare our results with previous studies (Section 3.5).

3.1 Spectral extraction

The pipeline that extracts the X-ray spectra of the *Chandra* detected sources consists of a collection of PYTHON modules that call CIAO 4.13 (Fruscione et al. 2006) routines. The extraction method is similar to the one described in Marchesi et al. (2016b), but modified to maximize the SNR of individual sources.

The *Chandra* survey of the COSMOS field consists of many overlapping observations (see Section 2.1). Each source is, therefore, typically present in several distinct *Chandra* pointings. The number of observations per source varies between 1 and 15, with a mode of 4. The best X-ray spectrum extraction region is then determined on the stacked image of each source and is defined as a circular region with a radius expressed in EEf that can have the value of 50, 60, 70, 80, 90, 95 per cent. The algorithm first extracts the source photons, C_S , within each EEf radii above. The background photons, C_B , are extracted from the stacked image within an annulus with an inner radius 2.5 arcsec larger than the adopted EEf radius and with a width of 17.5 arcsec. Any X-ray sources within the background region are masked out by excluding photons that lie within the selected EEf radius plus 2.5 arcsec. An additional requirement is that the background region includes at least 100 counts in the stacked image. If not, the outer radius is sequentially increased by 5 arcsecs until the condition is met. This process is graphically demonstrated in Fig. 1.

For each EEf value, we estimate the SNR as follows:

$$\text{SNR} = \frac{C_S - C_B \cdot R}{\sqrt{C_S + C_B \cdot R^2}}, \quad (1)$$

where R is the ratio between the areas of the source and background extraction regions. The number of counts is obtained using the `dmextract` and `get_counts` tasks of CIAO. The EEf value that maximizes the SNR in the full band is used to define the source and background extraction regions. The distribution of the selected EEf is shown on the left-hand panel of Fig. 2.

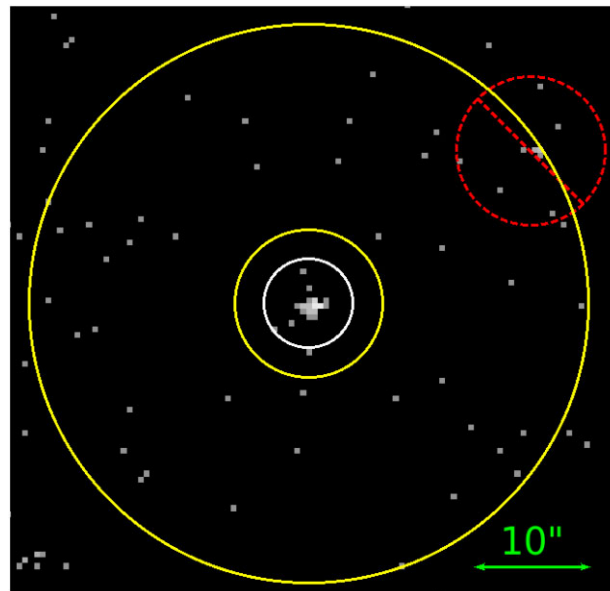


Figure 1. Example of a source and background X-ray spectral extraction regions for a radius set to EEf = 70 per cent. The source photon extraction region is represented by the white circle with a radius of 3.80 arcsec. The background photon extraction region is defined by the yellow annulus with an inner and outer radius of 6.30 and 23.80 arcsec, respectively. A nearby X-ray source partially overlaps with the background region in this example. The region around this source, indicated by the barred red dashed circle with a 6.34 arcsec radius, is masked out before extracting the background counts.

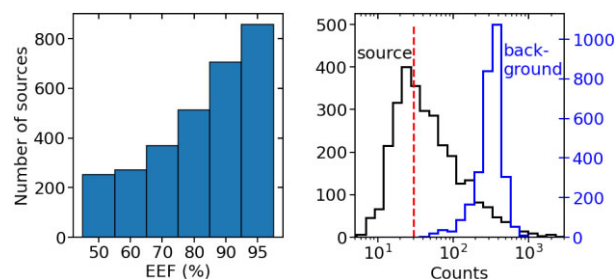


Figure 2. *Left-hand panel:* Distribution of the X-ray spectral extraction radius in EEf units for the *Chandra* COSMOS Legacy sources. *Right-hand panel:* The black histogram shows the distribution of the photon counts in the full band of the extracted X-ray spectra of our sources. The red vertical dashed line represents the 30 counts limit adopted by previous studies as the threshold above which the X-ray spectra are analysed (Marchesi et al. 2016b; Lanzuisi et al. 2018). The blue histogram shows the distribution of the photon counts in the full band of the extracted background spectra our sources.

The extraction regions of a given source are fed into the `specextract` task to extract the source and background spectra from each *Chandra*/ACIS-I observation that overlaps with the position of interest. The same task also generates the corresponding auxiliary response files (ARF) and redistribution matrix files (RMF). The ARF represents the efficiency of a detector as a function of the energy averaged over time. It is the product of the effective area and quantum efficiency. The effective area measures the detector's spatial size that is sensitive to photons of a given energy. The quantum efficiency measures the fraction of the incident photons that are registered by the detector as a function of the energy. The RMF describes how the energy of an incident photon is redistributed to the energy channels of the detector because of the imperfect charge

Table 2. X-ray spectral extraction properties of the sources. (1) source ID; (2–3) X-ray position; (4–5) optical counterpart position; (6) EEF used for extraction in per cent units; (7) source radius in arcsecond; (8) 0.5–7 keV net photon counts of the source; (9) the net photon counts of the background in all energy band; (10) flag indicating if the source is detected in the hard band (2–7 keV); (11) source ID in L18 if cross-matched. Full table electronically available.

ID (1)	RA (2)	Dec. (3)	RA_optical (4)	DEC_optical (5)	EEF (6)	radius_src (7)	cts_057 (8)	cts_bkg (9)	hard_flag (10)	ID L18 (11)
COSMOS_0_10	149.802	1.636	149.802	1.636	70	3.13	25	252	False	–
COSMOS_0_100	149.728	1.719	149.728	1.719	90	6.06	83	362	True	lid_1186
COSMOS_0_102	149.611	1.746	149.611	1.746	80	3.54	28	305	False	–
COSMOS_0_103	149.722	1.753	149.722	1.753	60	3.16	37	356	False	lid_2444
COSMOS_0_104	149.506	1.809	149.506	1.809	95	5.89	88	162	True	lid_970
⋮	⋮	⋮	⋮	⋮	⋮	⋮	⋮	⋮	⋮	⋮
COSMOS_8_95	150.398	2.797	150.398	2.797	90	4.19	54	312	True	lid_427
COSMOS_8_96	150.479	2.798	150.479	2.798	95	5.67	67	286	True	lid_401
COSMOS_8_97	150.454	2.806	150.454	2.806	95	5.3	295	314	True	lid_395
COSMOS_8_98	150.515	2.81	150.514	2.81	95	4.42	64	195	True	lid_410
COSMOS_8_99	150.672	2.811	150.672	2.811	50	2.32	28	116	False	lid_487

collection. The ARF and RMF calibration files are necessary for the X-ray spectral analysis. To obtain the final spectrum of a source, we combine the spectra extracted from the different observations by using the `combine_spectra` task. The source and background ARF and RMF calibration files are also combined by weighting by exposure time.

The right panel of Fig. 2 plots the distribution of the photon counts of the combined extracted X-ray spectra at the positions of *Chandra* COSMOS Legacy sources. The plot also shows the distribution of the photon counts of the corresponding extracted background spectra. As the 100 background counts threshold is applied on the stacked image, the background count can be lower after extraction because pointings with no photon counts in the source region are not extracted, even if the background region contains photon counts.

Previous X-ray spectral studies using the *Chandra* COSMOS Legacy observations have adopted a limit of 30 net counts in the X-ray spectrum for spectral analysis (Marchesi et al. 2016b; Lanzuisi et al. 2018). In our work, no such threshold is applied. Instead, we extract and analyse the X-ray spectra of all detected *Chandra* COSMOS Legacy sources. Among our 2965 X-ray sources (see Section 2.2), 1821 (61 per cent) have at least 30 counts, and 1141 (39 per cent) have less than 30 counts in the 0.5–7 keV band.

Table 2 is an extract of the table compiling the spectral extraction information on the 2965 sources of our sample. A full version of this table is available in electronic format.

3.2 X-ray spectral fitting algorithm

The extracted X-ray spectra are fitted using the Bayesian X-ray Analysis (BXA) package presented by Buchner et al. (2014). We assume an observed X-ray spectrum, D , and a spectral model, M , described by a set of parameters, Θ . In a Bayesian framework, the probability $\mathcal{P}(\Theta|D, M)$ of the parameter set given the observation and the model is

$$\mathcal{P}(\Theta|D, M) = \frac{\Pi(\Theta|M)}{\mathcal{Z}(D|M)} \mathcal{L}(D|\Theta), \quad (2)$$

where $\Pi(\Theta|M)$ is the prior knowledge of the parameter set for the chosen model. The model evidence, $\mathcal{Z}(D|M)$, is the probability of obtaining the observed data given the model. As it is independent of the specific parameters set of the model, it is the suited value to compare different models. This is an important feature of the Bayesian analysis that allows the selection of the model that best

represents the observations. The likelihood, $\mathcal{L}(D|\Theta)$, is the probability of obtaining the observed data for the set of model parameters. Fitting an X-ray spectrum usually involves the optimization of the likelihood to yield constraints on the spectral model parameters. However, nested sampling algorithms such as MLFriends (Buchner 2016, 2019), explore the entirety of the parameter space at once. They first draw parameter samples from the prior distribution and then iteratively replace the lowest likelihood points with new ones drawn from the prior with a higher likelihood. The posterior distribution is constructed from the removed points weighted by their likelihood and the parameter space volume they represent. This type of algorithm is capable of exploring large parameter spaces without getting stuck in local minima, and the returned posterior distribution fully encapsulates the uncertainties of the parameter estimation. The BXA package is using the MLFriends algorithm powered by the ULTRANEST package (Buchner 2021).

Ultra-nest works with any likelihood function. Because of the typically low number of photon counts of the X-ray spectra, in this work we estimate the likelihood using a Poisson log-likelihood function often referred to as the CSTAT statistic (Cash 1979). This is expressed as

$$\mathcal{L}_{\text{CSTAT}} = 2 * \sum_i M'(i) - C(i) [\ln C(i) - \ln M'(i)], \quad (3)$$

where $C(i)$ is the observed number of counts in the energy bin i and $M'(i)$ is the expected photon counts from the given model convolved with the RMF and multiplied by the ARF. The summation is over all the energy bins of the X-ray spectrum.

The extracted X-ray spectra at the positions of X-ray detections include contributions from both source and background photons. Therefore, the use of a Poisson likelihood for the X-ray spectral analysis requires modelling both components, i.e. including a model for both the source and background spectra. Therefore in equations (2) and (3), the spectral model, M , is the sum of the source, M_{source} , and background, M_{bkg} , models. The parameter set Θ also includes the background model parameters.

3.3 The UXCLUMPY spectral model

We choose to fit our observations with a physically motivated X-ray spectral model that is built upon the current knowledge of the distribution of matter in the vicinity of a black hole, which describes

the interaction of X-ray photons with the surrounding medium in a self-consistent way. Commonly used AGN-oriented physical X-ray spectral models include BNTORUS (Brightman & Nandra 2011) and MYTORUS (Murphy & Yaqoob 2009), both of which assume a cylindrically symmetric uniformly distributed obscuring medium and describe the transmission of X-ray photons through it. In this work, we opt for the UXCLUMPY torus model presented in Buchner et al. (2019). It simulates a toroidal-shaped obscuring medium which is, however, clumpy by nature and hence, consistent with the observations of eclipsing events that are believed to be responsible for the observed varying obscuration in the X-ray spectra of AGN (e.g. Risaliti, Elvis & Nicastro 2002). The clumpiness of the obscurer is also required by mid-infrared observations to explain, among others, the diversity of the observed SEDs or the strength of the 10 μm silicate feature (Ramos Almeida et al. 2009). The X-ray spectral model is constructed with XARS (Buchner et al. 2019), a radiative transfer code that computes the transmission of the photons emitted by the source and interacting with its surrounding material. The photons are collected in different inclination bins representing the LOS of the observer. It returns a complex spectrum that depends on both the source’s physical properties and the obscurer’s geometrical parameters.

The central source emits the photons with the energy distribution of a power law with a high-energy cut-off and is surrounded by spherical obscurers distributed in toroidal geometry. These obscurers represent clouds, and to each of them is assigned a fixed density that is drawn from a lognormal distribution with mean 10^{24} cm^{-2} and a standard deviation of 1 dex. The clouds are axisymmetrically dispersed and their number along the LOS to the observer decreases exponentially with the inclination towards the poles. Their radial distribution is uniform over two orders of magnitude. The radius of the clouds is distributed to reproduce the observed rate of the eclipsing events (Markowitz, Krumpe & Nikutta 2014). Each emitted photon has a probability of escaping without interacting with the medium. Such photons correspond to the transmitted component. As the column density along the LOS increases, the non-interaction probability decreases. When interacting with the medium, the photon can either be photoelectrically absorbed or be Compton-scattered. The reflected component corresponds to all photons that have been scattered at least once. At a certain high-energy threshold, the photoelectric absorption by neutral Fe can trigger a fluorescence process that emits photons at specific wavelengths, mainly at the FeK α emission line ($\sim 6.4 \text{ keV}$). Photons produced this way constitute the fluorescent-line component of the UXCLUMPY model. At energies higher than 10 keV, an excess of photons is often observed in the curvature of the spectrum peaking at 20–30 keV and is due to Compton scattering (Elvis 2000). This so-called Compton hump requires an additional obscurer that reflects the intrinsic AGN emission towards the observer without being affected by clouds of the clumpy torus (Ramos Almeida & Ricci 2017). In UXCLUMPY, this obscurer is modelled as a ring of CTK ($N_{\text{H}} > 10^{24} \text{ cm}^{-2}$) clouds that are in contact with each other forming a thick doughnut-shaped structure around the central engine.

In obscured Seyfert galaxies in the local Universe, an excess of soft X-ray photons is often observed in their spectra (Bianchi, Guainazzi & Chiaberge 2006). This is believed to be produced by the elastic scattering of photons emitted by the AGN onto photoionized gas clouds located above the obscurer and thus not interacting with it. The photons collected after this process belong to the soft or Thomson scattering component, and their spectrum mirrors the intrinsic spectrum (power-law spectral shape) emitted by the central engine.

Table 3. Table summarizing the input parameters of the UXCLUMPY model and their prior used in our analysis.

Parameter	Prior
CTKcover	Fixed = 0.4
TORsigma	Fixed = 28°
Inclination	Fixed = $18.2^\circ / 45^\circ / 70^\circ$
E_cutoff	Fixed = 200 keV
Photon index	Gaussian(1.95, 0.15)
$\log(\frac{N_{\text{H}}}{\text{cm}^{-2}})$	Uniform(20, 26)
$\log(\text{norm.torus})$	Uniform(-8, 3)
$\log(\text{norm.scattering})^a$	Uniform(-7, -1.5)
Redshift spectroscopic	Fixed
Redshift photometric	Photometric PDF
No redshift estimation	Uniform(0, 6)
$\log(\text{norm.background})$	Uniform($\text{init.val}^b \pm 2$)

^aThe logarithmic norm of the soft scattering component corresponds in reality to $\log(\text{norm.torus}) + \log(\text{norm.scattering})$. ^bThe init.val corresponds to the initial background normalization value computed by the `automatic_background()` command and re-scaled to the source area.

In summary, the spectral components included in our modelling based on the UXCLUMPY implementation are (i) the transmitted X-ray component, (ii) the reflected component, (iii) the fluorescence emission lines, and (iv) the soft energy excess emission. The three first components are merged in a single table model, whereas the Thomson scattering component is in a second and optional table. The parameters of this additional table model are linked to the parameters of the main table (i.e. redshift, power-law index of the obscurer) except for the normalization, which is left free to vary. Galactic absorption is further applied to the components above. We choose to fix the Galactic column density for all sources to the average N_{H} value in direction of the COSMOS field, $1.72 \times 10^{20} \text{ cm}^{-2}$ (Kalberla et al. 2005).

The UXCLUMPY model has several geometrical and physical parameters impacting the spectrum shape. The exponential inclination distribution of the absorbers around the central source is characterized by the TORsigma parameter varying between 0 deg, an infinitesimally thin torus, and 84 deg, almost a sphere. The ring of CTK absorbers is characterized by its covering factor, the CTKcover parameter, varying between 0, an infinitesimally thin equatorial disc, and 0.6, where the large equatorial CTK clouds cover 60 percent of the lines of sight. The inclination angle parameter of UXCLUMPY controls the position of the observer relative to the vertical (symmetry) axis of the adopted torus geometry. The UXCLUMPY table model allows three broad bins of inclination angles 0–30 deg (face-on), 30–60 deg (intermediate), and 60–90 deg (edge-on), each of which includes a wide range of LOS column densities. Due to degeneracies with the rest of the model parameters, CTKcover and TORsigma are difficult to constrain even for high photon counts sources. In our analysis, we fix the CTKcover and TORsigma parameters to their default values, 0.4 and 28, respectively (see Table 3). These values are obtained by fitting the X-ray spectra of local AGN (Buchner et al. 2019). In our baseline implementation, we further fix the inclination angle parameter to be 45 deg, in the range intermediate inclination bin, but we also explore and quantify the sensitivity of our results to this choice.

We fit our sample with six different set-ups of the X-ray spectral model. The first one is the sum of the torus model and the soft scattering component with an inclination angle of 18.2 deg with respect to the symmetry axis (face-on). The second and third model variants are the same as above but with an inclination angle of 45

(intermediate) and 70 deg (edge-on), respectively. We also consider three additional model set-ups identical to those above but without the soft scattering component. The comparison between the different model set-ups is discussed in detail in the following sections.

In all our model set-ups, the cut-off energy of the power law emitted by the central engine is fixed to 200 keV. During the fit, we have several free parameters to which we assign different priors (listed in Table 3): the normalization of the torus component with a log-uniform prior, the photon-index of the power law with a Gaussian prior, the total LOS column density with a log-uniform prior and if necessary, the normalization fraction of the scattering component with also a log-uniform prior. Uniform and log-uniform are neutral priors, only their upper and lower limits are significant and have been chosen to be reasonable. The normalization of the soft scattering component is set to be equal, at the maximum, to $10^{-1.5}$ of the direct component normalization. The Gaussian prior of the photon index, centred at 1.95 with a standard deviation of 0.15, is motivated by nearby AGN observations (Nandra et al. 1997). In the spectral fits, the redshift parameter of the UXCLUMPY model is fixed to the sources' spectroscopic redshift. If this is not available, the photometric redshift probability distribution function (PDF) is provided to BXA as prior to the redshift parameter. If a source has no redshift estimation, a uniform prior between 0 and 6 is adopted.

As the spectrum is a combination of the source and background photons, the latter must also be modelled. In this work, we use the `automatic.background()` command from BXA to model it (Simmonds et al. 2018). This machine-learning-based approach trained itself on large X-ray surveys to derive the principal components describing the background and its variations. When called, this function fits the background spectrum with the principal component models and progressively increases their complexity. It verifies the background fitting improvement by using the Akaike information criterion. It finally returns the best background fit model that has all its parameters frozen except for the normalization, which is added to the free-parameter set of the full model. All the parameters are indicated in Table 3.

By fitting the extracted spectra between 0.5 and 8 keV using BXA with UXCLUMPY as the model, we constrain the free parameters in a Bayesian framework. The choice of energy limits does not impact significantly the results. Fig. 3 shows an X-ray source of our catalogue with its best-fitting model, and its different components. The error margins are computed from the parameter posterior distribution and represent their 1σ variation. The choice of the source is primarily justified by its relatively high photon counts, 116, in the 0.5–7 keV band, and by its significant scattering component.

3.4 Comparison between different set-ups

We explore the six set-ups of the UXCLUMPY X-ray spectral model with different fixed parameters and components described in Section 3.3 (see Table 3), to assess their impact on the final results and determine the one to be used as the baseline model further in our analysis.

As discussed in Section 3.2, the model evidence \mathcal{Z} is the best tool to compare two models with the same data set. The larger it is the more favoured is the corresponding model. We adopt a logarithmic evidence difference $\Delta \log \mathcal{Z} > 4.6$ as the threshold to select strongly favoured models (Jeffreys 1961). Additionally, we consider that a difference below this threshold still favours the highest evidence model but we cannot rule out the alternative model.

Table 4 presents the comparison of the different UXCLUMPY X-ray spectral model set-ups. For individual sources we estimate

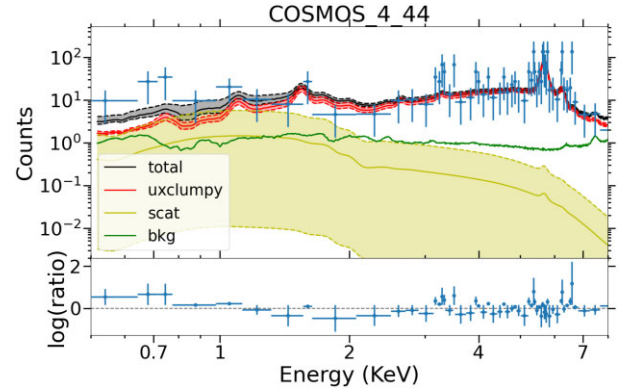


Figure 3. Example of X-ray spectral analysis result using BXA with the UXCLUMPY model. The blue crosses are the extracted X-ray spectrum grouped to yield an SNR above 1 per bin. The red line corresponds to the UXCLUMPY model, the yellow line represents the soft scattering, and the green line is the background model. The sum of all three components above is shown with the black line. The shaded regions correspond to the 1σ confidence interval of the corresponding component. The lower panel plots the logarithmic ratio between the X-ray spectrum and the best-fitting model as a function of the energy.

Table 4. Table presenting the evidence comparison between the different model set-ups relative to our baseline model that includes Thomson scattering and has an inclination angle of $i = 45^\circ$. The second column is the ensemble evidence difference relative to the baseline model. The ensemble evidence of a given model is defined as the sum of the evidences of individual X-ray sources and is listed in brackets. The error bars are estimated by bootstrapping (see the text for details). The third column displays the number of individual sources having a higher evidence than the baseline model and in parentheses is the number of sources for which the model is strongly favoured over the baseline model. Similarly, the last column indicates the number of individual sources with lower evidence, and in parentheses, the number of sources for which the model can be ruled out.

Models	Sum difference (Sum total)	$\Delta \log \mathcal{Z} \geq 0$ ($\Delta \log \mathcal{Z} > 4.6$)	$\Delta \log \mathcal{Z} < 0$ ($\Delta \log \mathcal{Z} < -4.6$)
$i = 18.2^\circ$	18.7 ± 12.3	1514	1451
Scattering	(-1120795.3)	(0)	(0)
$i = 18.2^\circ$	-153.7 ± 41.7	1426	1539
No scattering	(-1120965.7)	(0)	(4)
$i = 45^\circ$	0	2965	0
Scattering	(-1120814.3)	(0)	(0)
$i = 45^\circ$	-201.5 ± 39.7	1353	1612
No scattering	(-1121013.0)	(0)	(5)
$i = 70^\circ$	-40.7 ± 11.3	1389	1576
Scattering	(-1120855.8)	(0)	(0)
$i = 70^\circ$	-256.3 ± 42.6	1303	1662
No scattering	(-1121080.5)	(0)	(7)

the logarithmic evidence difference, $\Delta \log \mathcal{Z}$, between each model set-up and the one with soft-scattering and an inclination angle of 45 deg (baseline model). For a given model set-up, we sum up the logarithmic evidence differences of all the sources (following Buchner et al. 2014) and compute its uncertainty using a bootstrap resampling method. It consists of taking N sources with replacement with N being the number of sources in our sample and calculating the sum of the logarithmic evidence differences relative to the baseline model. This process is repeated 100 times for each model set-up. The standard deviation of $\Delta \log \mathcal{Z}$ estimated from these 100 trials

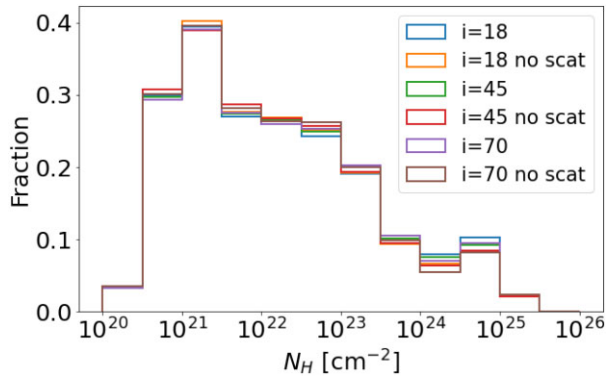


Figure 4. N_{H} distribution for different inclination angles and scattering parameters in the UXCLUMPY model. There are no significant differences between the different model set-ups.

Table 5. CTK sources for each X-ray spectral model set-up. The first and second columns provide a description of the model set-up. The third column is the number of sources with median posterior $N_{\text{H}} > 10^{24} \text{ cm}^{-2}$ and, in parenthesis, the fraction of the total sample it represents. Finally, the last column shows the averaged fraction of the N_{H} posterior distributions above the CTK limit.

Inclination (deg)	Soft scattering	Number of CTK sources	Fraction of CTK chains (per cent)
18.2	Yes	302 (10.2 per cent)	10.9
18.2	No	266 (9.0 per cent)	9.2
45	Yes	280 (9. per cent)	10.5
45	No	251 (8.5 per cent)	8.6
70	Yes	281 (9.5 per cent)	10.5
70	No	238 (8.0 per cent)	8.2

represents the uncertainty of the logarithmic evidence difference of a given model set-up. The table also shows the total number of individual X-ray spectra with $\Delta \log \mathcal{Z} > 4.6$ or $\Delta \log \mathcal{Z} < -4.6$ relative to the baseline model, in other words, how many times a model set-up is strongly favoured or disfavoured relative to the baseline model.

Table 4 shows that the Thomson scattering component is strongly favoured by the data. The total logarithmic evidence of the model set-ups with the scattering component are larger by typically 100 compared to the same model without the scattering. Moreover, the 18.2 deg inclination is slightly favoured with a $\log \mathcal{Z}$ difference of 18.7 ± 12.3 , although the uncertainty is large. The 70 deg inclination is performing worse with a $\log \mathcal{Z}$ difference of -40.7 ± 11.3 .

We compare the column density distributions obtained by the different model set-ups in Fig. 4. These histograms are constructed using the median of the corresponding N_{H} posterior distribution for each source. The resulting N_{H} distribution is not sensitive to the adopted model set-up. Table 5 further explores differences in the total number of CTK AGN among the diverse model set-ups. The number of CTK sources decreases slightly with the increasing inclination angle, but overall, all six models yield similar numbers of CTK sources. Moreover, most of these CTK sources (a total of 222) are common in all six model set-ups. The fraction of CTK sources also decreases by 1 per cent when the model does not have a scattering component. One can also look at the posterior distribution instead of the median values to get a more nuanced estimation of the

Compton-thickness of the sample. We simply average the fraction of the posterior distribution in the CTK regime for each source. We see that the similarities among the different model set-ups are maintained.

Based on the analysis above, our baseline X-ray spectral model includes a soft-scattering component, which is strongly favoured by the data, and assumes an inclination angle fixed to 45 deg. Although the evidence analysis shows a weak preference for lower inclinations angles (18.2 deg; nearly face-on orientation), we opt for the intermediate group of sightlines in UXCLUMPY (the 30–60 deg bin) that probe a wider range of columns densities between the central engine and the observer. Fig. 4 nevertheless demonstrates that our results are not sensitive to the inclination angle choice.

3.5 Comparison with previous studies

This section compares the physical parameters inferred by our X-ray spectral analysis with those derived in previous studies using the *Chandra* Legacy data. Since one of the main motivations of our work is the characterization of the LOS obscuration of AGN, we limit this comparison to the hydrogen column density. Marchesi et al. (2016b) fit the X-ray spectra of *Chandra* Legacy sources with more than 30 net counts in the 0.5–7 keV band using a power-law spectral model modified by photoelectric absorption. The adopted model is valid for moderately obscured AGN ($N_{\text{H}} \lesssim 10^{23} \text{ cm}^{-2}$) but becomes increasingly inaccurate for higher levels of obscuration. This is because of the increasing importance of the Compton scattering for $N_{\text{H}} \gtrsim 10^{23} \text{ cm}^{-2}$ and degeneracies between the fitted parameters, i.e. power-law photon index and absorbing column density. Lanzuisi et al. (2018, L18 hereafter) updates the spectral analysis results of Marchesi et al. (2016b) for sources that show evidence for high levels of LOS obscuration. AGN with an estimated spectral index < 1.4 or a hydrogen column density $N_{\text{H}} > 10^{23} \text{ cm}^{-2}$ are selected. This subsample is refitted using the MYTORUS physically motivated model (Murphy & Yaqoob 2009) that includes processes such as Compton scattering and fluorescent line emission assuming a toroidal obscurer geometry. L18 presents the physical properties of 1832 sources within the *Chandra* Legacy survey. It includes the original results of Marchesi et al. (2016b) updated with the MYTORUS model fitting results for the obscured candidates. This catalogue is cross-matched with ours within 1.7 arcsec to yield a total of 1805 common sources. A larger radius would not significantly increase the source numbers (1814 sources at 2 arcsec) and would lead to source misidentification with several sources matched to the same source.

Fig. 5 compares the N_{H} values obtained for our baseline model using BXA with those from L18. At moderate obscuration, there is overall good agreement between the independently estimated N_{H} values. The L18 spectral catalogue also includes a large number of AGN for which the absorbed power-law fits of Marchesi et al. (2016b) yield an upper limit to the column density. The bulk of these sources are associated with unobscured AGN in our spectral analysis, with column densities $N_{\text{H}} \lesssim 10^{22} \text{ cm}^{-2}$. Fig. 5 further shows that it is in the CTK regime that the most significant discrepancies between our results and those of L18 appear.

There are 34 L18 sources with best-fitting N_{H} in the CTK regime compared to 75 AGN in our analysis with median hydrogen column densities distribution $N_{\text{H}} > 10^{24} \text{ cm}^{-2}$ (19 in common). Many of the 75 sources have broad N_{H} PDFs that extend below 10^{24} cm^{-2} into the CTN regime but still heavily obscured. As an example, the N_{H} PDF of the source COSMOS.1.420 is represented by the upper histogram in Fig. 6. It shows two distinct peaks, one below $N_{\text{H}} = 10^{24} \text{ cm}^{-2}$ and a flatter one above this limit. Multinested-sampling

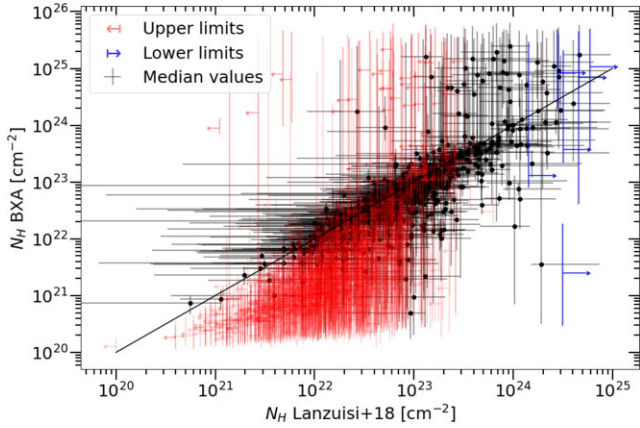


Figure 5. N_{H} values from our model compared to the best-fitting N_{H} values from L18. The black dots represent the median values of our BXA fit estimations and their errorbars represent their 1σ uncertainties. The red (blue) arrows are upper (lower) N_{H} estimates in L18.

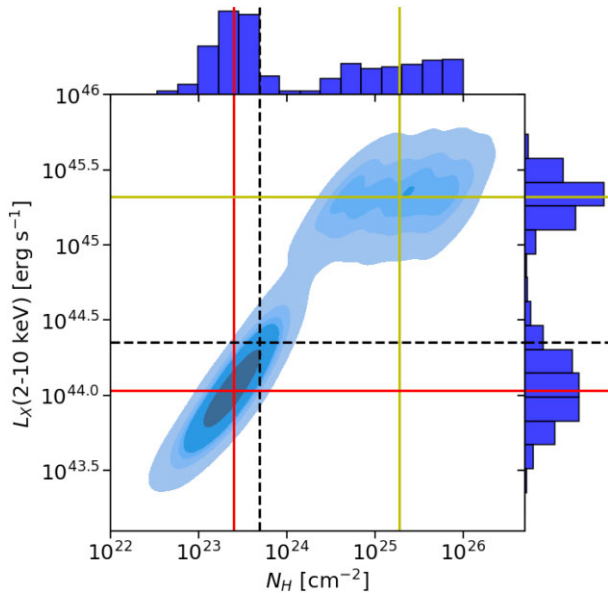


Figure 6. Density plot of the posterior probability distribution of the X-ray luminosity $\log L_X(2-10 \text{ keV})$ as a function of the column density $\log N_{\text{H}}$ for the source COSMOS_1_420. The one-dimensional projections of the posterior on the X-ray luminosity and column density axes are shown on the right and top panels, respectively. The median values are plotted in dashed black lines, whereas the CTN and CTK median solutions are plotted with the red and yellow solid lines, respectively.

algorithms like ULTRANEST used by BXA allow us to explore such posterior distributions efficiently. Standard Markov Chain Monte Carlo algorithms may get stuck in one of the local minima and hence yield unimodal posteriors that do not represent the complexity of the system.

Point parameter estimates, like the median N_{H} value plotted in Fig. 5, are problematic in the case of a multimodal PDF (e.g. Fig. 6). Instead, for this class of sources it is more instructive to show both peaks of the PDF. We first define double-peaked sources as those for which the posterior N_{H} distribution includes at least 25 per cent CTK and CTN solutions. For these sources, both N_{H} peaks (connected with a line) are compared in Fig. 7 with the best-fitting N_{H} inferred by L18. In most cases, the one-to-one relation is bracketed by two

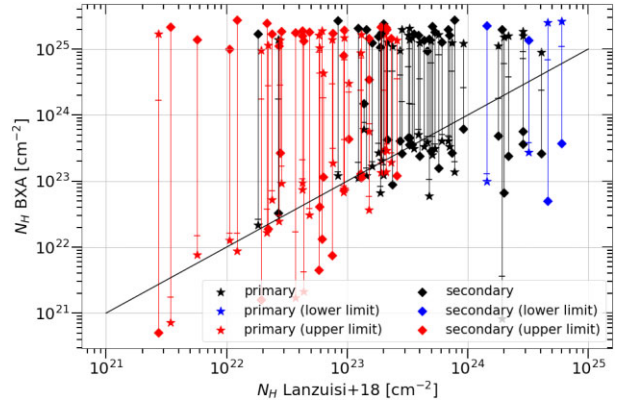


Figure 7. Comparison between the best-fitting N_{H} determined by L18 and our estimates for AGN with a bi-modal N_{H} posterior PDF in our analysis. For each source, both peaks are plotted and connected with a line. The symbols associated with each peak represent the likelihood of that solution, i.e. the fraction of the posterior associated with the peak in question. Stars represent primary peaks (more likely), whereas diamonds indicate the secondary (less likely) peaks of the posterior. The horizontal bars on the lines connecting two peaks indicate the median of the N_{H} posteriors. The red and blue colours represent sources that have upper and lower N_{H} limits in L18, respectively. The black colours correspond to the best-fitting N_{H} values in L18.

peaks of the posterior distribution function. We also notice that for a fraction of the double-peaked sources, the CTK part of the posterior distribution function results from small count statistics as 66 per cent of the double-peaked sources have less than 30 counts in the full band. The bi-modality of the posterior distribution can also be an effect of spectral model degeneracies, like the level of obscuration and the intrinsic X-ray luminosity. One option to break the degeneracies would be to use multiwavelength information to add parameter priors into the spectral analysis to better constrain the physical properties of the sources. This approach is presented in the next section.

4 X-RAY SPECTRAL FITTING IMPROVEMENT WITH MULTIWAVELENGTH INFORMATION

In the previous section, several sources were identified with broad or multimodal column density posterior distributions, resulting from degeneracies between model parameters and small photon statistics. Fig. 6 plots the posterior distribution in the two-dimensional space of X-ray luminosity and obscuring hydrogen column density for the double-peaked source COSMOS_1_420. The bi-modality in the column density posterior distribution is also seen in the X-ray luminosity PDF of this source. There is a strong positive correlation between these two parameters in the sense that the inferred $L_X(2-10 \text{ keV})$ increases with increasing column density. Indeed, a higher column density requires a higher intrinsic accretion luminosity to compensate for the stronger photon absorption and reproduce the observed source flux. An independent estimate of the intrinsic AGN luminosity could therefore provide additional constraints on the X-ray spectral analysis posterior distributions and help break the degeneracies shown in Fig. 6.

The intuition that X-ray and IR luminosities and LOS obscuration are correlated is not recent, numerous studies in the last 30 yr attempted to identify heavily obscured AGN by looking for sources that appear X-ray underluminous for the mid-infrared or optical emission (Risaliti et al. 1999; Alexander et al. 2008; Georgantopoulos et al. 2011). We build upon previous studies but instead of applying strict and arbitrary cuts on the X-ray and IR luminosities ratio

to dictate whether a source is CTK or not, we are using the IR luminosity only as a prior in our X-ray spectral analysis. For that purpose, we use the mid-IR νF_ν luminosity at $6\ \mu\text{m}$ to estimate the intrinsic (unabsorbed) accretion luminosity that is then converted to the intrinsic X-ray luminosity via well-established correlations (e.g. Stern 2015; Mateos et al. 2015; Chen et al. 2017). The IR-derived X-ray luminosity and uncertainties are then used as a prior to guide the X-ray spectroscopy and improve constraints on the measured obscuration. Our Bayesian approach combines the uncertainties of each measure and proxy relationships in a consistent way throughout our analysis, improving the confidence of our results.

The next sections describe how templates fits to the observed SEDs of *Chandra* COSMOS Legacy sources are used to constrain the AGN mid-IR luminosity and how this information feeds back to the X-ray spectral analysis to break parameter degeneracies.

4.1 SED-fitting methodology

SED template fitting is an efficient tool to recover the emission associated with the AGN accretion luminosity, even when the AGN component does not dominate the SED. Observations at mid- and far-IR wavelengths are necessary to separate the AGN emission from the thermal radiation produced by stellar processes. Therefore, we cross-match the positions of the optical counterparts of the *Chandra* COSMOS Legacy survey X-ray sources with the ‘super-deblended’ far-IR to (sub)millimetre photometric catalogue of Jin et al. (2018, see Section 2.2). In this exercise, a matching radius of 1.3 arcsec is adopted. For the density of IR sources ($\sim 10^5\ \text{deg}^{-2}$), this search radius corresponds to a spurious fraction of 5.1 per cent. Among the 2965 X-ray sources in our sample, 164 have no counterpart in the Jin et al. (2018) catalogue. From the remaining 2801 IR associations, 9 sources have redshifts above 4, which is the upper redshift limit of the SED-fitting algorithm. These sources have not been analysed and are excluded from the sample. This leaves a total of 2792 X-ray sources of *Chandra* COSMOS Legacy that have been matched with Jin et al. (2018) counterparts and fulfil the redshift criterion for the SED fit.

We fit the 2–500 μm SED of the matching sources using the multicomponent Bayesian SED-fitting package FORTESFIT¹ (Rosario 2019). Our choice of fitting algorithm is motivated by its Bayesian nature. Indeed, the decomposition of the AGN and star formation contributions in the IR part of the SED is not trivial depending on the choice of templates to use and degeneracies between model parameters. However, FORTESFIT and its Bayesian inference methodology are designed to tackle these issues and capture the uncertainties of the inferred parameters. These uncertainties are then consistently propagated to the X-ray spectral analysis. Moreover, we measure the IR luminosity at $6\ \mu\text{m}$, where the contrast between the host galaxy star formation and the AGN torus IR emissions is typically large (e.g. Nardini et al. 2008, 2009), thereby facilitating the decomposition. We also choose to use state of the art observationally motivated model templates that are able to capture the observed diversity of AGN and star formation emission in the infrared. Our SED modelling includes the unabsorbed stellar emission from Bruzual & Charlot (2003), the IR emission coming from the torus based on the empirical DECOMPIR AGN model (Mullaney et al. 2011), and the IR emission from the dust-obscured star formation (Dale et al. 2014). The stellar emission template has the age and mass of the stellar population as free parameters. As our aim is not to constrain the

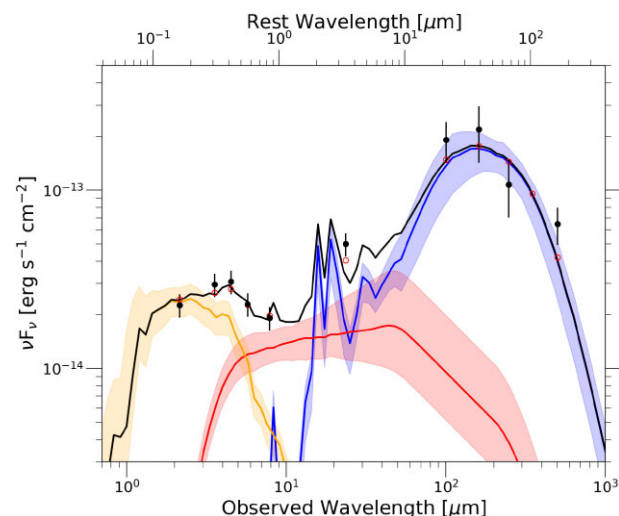


Figure 8. Example of a template fit to the IR SED of the X-ray source COSMOS_1_420 (object with ID 10178753 in the Jin et al. (2018) catalogue) using the FORTESFIT code. The black dots and vertical lines represent the photometry of the source and its uncertainties. The curves represent the stellar population emission (orange), the IR AGN emission (red), and the IR emission from star formation (blue). The shaded regions represent the approximate 1σ scatter of each SED component as constrained by FORTESFIT. The black curve corresponds to the sum of the above three components.

stellar population emission but only to consider its possible excess at rest-frame IR wavelengths that could affect the fit of the AGN emission, we do not include optical/UV photometry in our SED fits. Including optical/UV photometry does not significantly impact the AGN emission constraints and the final results within the error margins. The free parameters of the star-forming galaxy model are the 8–1000 μm galaxy luminosity from star formation, L_{SF} , and a shape parameter that describes a wide range of spectral shapes for normal star-forming galaxies. The DECOMPIR template combines a broken power law and a black body. The free parameters are the IR AGN luminosity in the interval 8–1000 μm and the short-wavelength slope, which we vary freely in the $[-0.3, 0.8]$ range following Mullaney et al. (2011). For more details on the SED-fitting process, we refer to Andonie et al. (2022). Fig. 8 shows the SED template fit of the double-peaked X-ray AGN previously shown in Fig. 6. The emission contributions of the stellar population, AGN torus and star formation and their 1σ uncertainties estimated by FORTESFIT are overplotted in the figure.

4.2 Integration of the $L_{6\ \mu\text{m}}$ measurements into the X-ray spectral analysis

The FORTESFIT SED code samples the $L_{6\ \mu\text{m}}$ luminosity PDF at the 1st, 16th, 50th, 84th, and 99th percentiles. These point estimates are linearly interpolated to reconstruct the $L_{6\ \mu\text{m}}$ luminosity PDFs of the individual AGN of the sample. We caution that the SED-fitting approach becomes less efficient in constraining the intrinsic AGN properties if they are weak relative to the stellar emission of the host galaxy. During the SED fit, the AGN $L_{8-1000\ \mu\text{m}}$ luminosity is a free parameter that has a lower limit of $10^{38}\ \text{erg s}^{-1}$. Many X-ray sources have posterior $L_{8-1000\ \mu\text{m}}$ AGN luminosities that are skewed to this lower boundary. For these sources, the AGN component is essentially not needed to fit the observed SED or, equivalently, the AGN template has a much lower normalization than the dusty star formation component. In these cases, we use the posterior distribution

¹<https://github.com/vikalibrate/FortesFit>

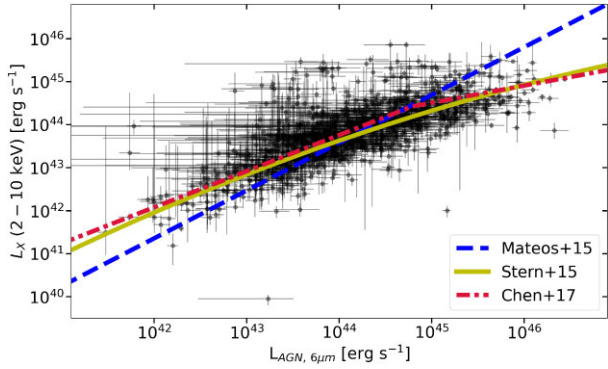


Figure 9. AGN X-ray luminosity in the 2–10 keV band (obscuration corrected) versus the AGN νF_ν luminosity at 6 μm . The latter is estimated from the template fits to the observed SED of the X-ray sources in the *Chandra* COSMOS Legacy field. We choose not to plot the 6 μm luminosity upper limits for the sake of clarity. Sources with multimodal X-ray luminosity posteriors are also not plotted for the same reason. The dashed blue, solid yellow and dash-dotted red lines correspond, respectively, to the Mateos et al. (2015), Stern (2015), and Chen et al. (2017) $L_X(2\text{--}10\text{ keV})\text{--}L_{6\mu\text{m}}$ relationships.

to determine the 3σ upper limit to the intrinsic AGN luminosity. The empirical criterion adopted to identify such sources is that the 1st percentile of the posterior is lower than $2 \times 10^{38} \text{ erg s}^{-1}$. With this criterion, among the 2792 sources with an SED fit, 1367 are constrained, and 1425 are assigned 3σ upper limits.

Fig. 9 shows the $L_X(2\text{--}10\text{ keV})$ as a function of the $L_{6\mu\text{m}}$ for the X-ray sources in the *Chandra* COSMOS Legacy survey. As already demonstrated in previous studies, these two luminosities are well correlated indicating that $L_{6\mu\text{m}}$ can be used as a proxy for the intrinsic $L_X(2\text{--}10\text{ keV})$. Rather than deriving a relation between the X-ray luminosity and the 6 μm luminosity from the data plotted in Fig. 9, we choose to use published relations and test which one describes best our observations. Three recent parametrizations for the $L_{6\mu\text{m}}\text{--}L_X(2\text{--}10\text{ keV})$ correlation are shown in Fig. 9. These curves correspond to equation (4) for the Chen et al. (2017) relation, equation (5) in the case of the Mateos et al. (2015) work, and equation (6) for the Stern (2015) sample:

$$l_x(l_{6\mu\text{m}}) = \begin{cases} 0.84 \cdot (l_{6\mu\text{m}} - 45) + 44.6 & \text{if } l_{6\mu\text{m}} \leq 44.79 \\ 0.40 \cdot (l_{6\mu\text{m}} - 45) + 44.51 & \text{if } l_{6\mu\text{m}} > 44.79, \end{cases} \quad (4)$$

$$l_x(l_{6\mu\text{m}}) = 0.377 + 0.90 \cdot (l_{6\mu\text{m}} - 44) + 44, \quad (5)$$

$$l_x(l_{6\mu\text{m}}) = 40.981 + 1.024 \cdot (l_{6\mu\text{m}} - 41) - 0.047 \cdot (l_{6\mu\text{m}} - 41)^2, \quad (6)$$

with $l_x = \log(L_X \text{ erg s}^{-1})$ and $l_{6\mu\text{m}} = \log(L_{6\mu\text{m}} \text{ erg s}^{-1})$.

Fig. 10 shows the offsets distribution between the measured L_X and the predicted X-ray luminosity for each of the three relations listed above. The offset is the difference between the median of the $\log L_X(2\text{--}10\text{ keV})$ posterior distribution and the predicted logarithmic luminosity by each relation using the inferred $L_{6\mu\text{m}}$ of the sources. The ΔL_X distributions are fit with a Gaussian to infer the corresponding mean and scatter. The best-fitting parameters are also shown in Fig. 10. The relations of Chen et al. (2017) and Stern (2015) show a narrower dispersion of the ΔL_X distributions than the one by Mateos et al. (2015). Besides, our observations show systematic offsets relative to the Chen et al. (2017) or Mateos et al. (2015) relations. This is smaller in the case of the Stern (2015) relation. We have confirmed that fitting a second order polynomial to the data points shown in

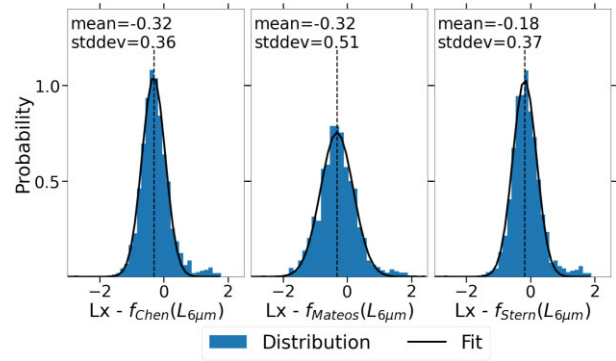


Figure 10. Distribution of the difference between the median $\log L_X(2\text{--}10\text{ keV})$ of the posterior distribution derived by the X-ray spectral analysis and the expected $\log L_X(2\text{--}10\text{ keV})$ determined from the AGN $L_{6\mu\text{m}}$ using the relationships of Chen et al. (2017) (left-hand panel), Mateos et al. (2015) (middle panel), and Stern (2015) (right-hand panel). The best-fitting normal distributions are also shown (black curves), with their parameters (mean and standard deviation) are also indicated in each panel.

Fig. 9 yields a $L_{6\mu\text{m}}\text{--}L_X(2\text{--}10\text{ keV})$ relation similar to that of Stern (2015). Since the AGN sample used in Stern (2015) is larger than ours, spans a broader luminosity baseline and is independently selected, we choose to use their $L_{6\mu\text{m}}\text{--}L_X(2\text{--}10\text{ keV})$ correlation in our analysis. Our final results and conclusions are not sensitive to that choice.

For the SED constrained sources, we convert the $L_{6\mu\text{m}}$ luminosity PDFs into a $L_X(2\text{--}10\text{ keV})$ PDF by using the Stern (2015) relation. We account for the dispersion of this relation by convolving the inferred PDFs with a Gaussian with a 0.4 dex logarithmic standard deviation. The latter value is the dispersion estimated by Stern (2015) and is similar to the standard deviation of our ΔL_X distribution in Fig. 10. In the case of 6 μm AGN luminosity upper limits, we assume that all luminosities below the 3σ upper limits are equiprobable. For this reason, we consider the $L_{6\mu\text{m}}$ PDFs to be log-uniform below the upper limits and have a zero-probability for brighter luminosities. We also apply the Stern (2015) relation on it and convolve it with the best-fitting Gaussian to obtain the L_X prior.

The X-ray luminosity is not one of the free parameters of the UXCLUMPY model. Therefore, we translate the X-ray luminosity prior to the UXCLUMPY normalization parameter prior, which is then applied to the BXA spectral fits. We can then reprocess the X-ray spectra adding the mid-IR information for the selected X-ray AGN. This prior aims to improve the characterization of highly obscured AGN and only minimally disrupt the X-ray spectral fits. We, therefore, choose to apply it only to potential CTK sources, defined as those with at least 5 per cent of their posterior N_{H} distribution being above the CTK limit, 10^{24} cm^{-2} . This definition is the same as in L18. Changing this cut to 1 per cent or 10 per cent has little impact on the final results. There are 829 CTK candidates among our sources, but 54 of them do not have an IR-counterpart in Jin et al. (2018) catalogue. We then apply our methodology to a sample comprising 775 sources, of which 314 have constrained priors and 461 have upper limits priors.

For the same source shown in Figs 6 and 8, Fig. 11 demonstrates how the $L_{6\mu\text{m}}$ -based prior breaks the X-ray spectral modelling degeneracies and improves the column density constraints. Before applying the $L_{6\mu\text{m}}$ -based prior, there is a total of 300 sources with broad or multimodal X-ray analysis posteriors and IR counterparts. After, only 16 of them remained with multimodal/broad posteriors.

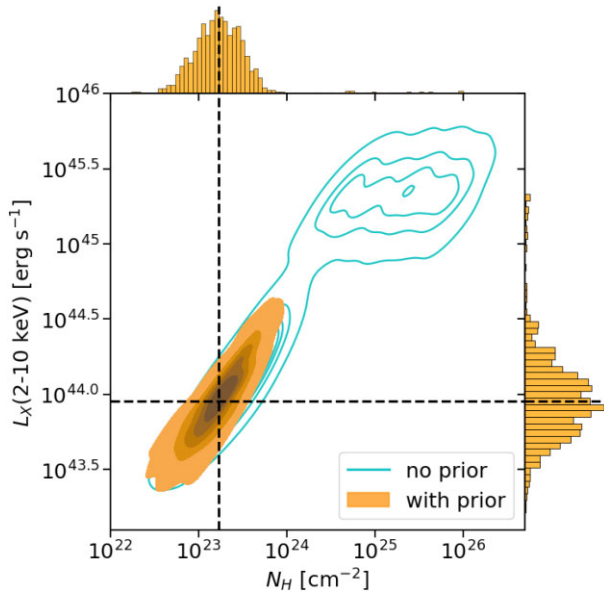


Figure 11. Density plot of the posterior distribution of the X-ray luminosity $\log L_X(2-10 \text{ keV})$ as a function of the column density $\log N_H$ for the source shown in Figs 6 and 8. The parameter posterior distributions are obtained by X-ray spectral analysis using the $L_{6 \mu\text{m}}$ -based luminosity prior. The 1-dimensional projections of the posterior on the X-ray luminosity and column density axes are shown on the right and top panels, respectively. The median values are plotted in dashed black lines. The posterior distribution of the fit without the use of prior is plotted as cyan contours in the background.

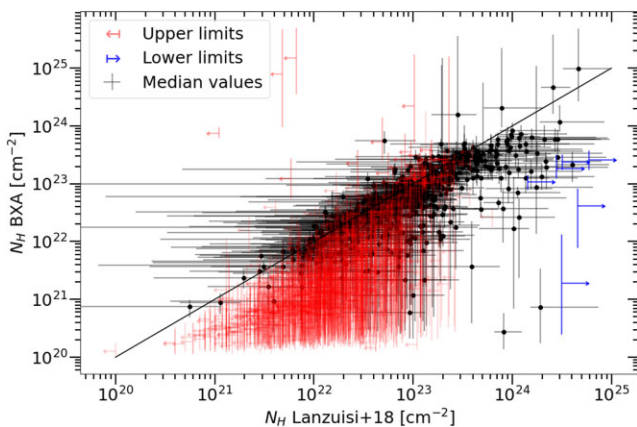


Figure 12. Comparison of the N_H values derived from our spectral analysis using the $L_{6 \mu\text{m}}$ prior (vertical axis) with those derived by L18 (horizontal axis). The black dots represent the median values of our spectral fit estimations. The red (blue) arrows are upper (lower) limits in L18.

15 of these sources have less than 35 photons in their X-ray spectra. The lack of certainty in these cases is not surprising, but our methodology none the less helps constrain the physical parameters of the bulk of the population.

In Fig. 12, the N_H values obtained from the fit using priors are plotted against the values of L18. The figure is similar to Fig. 5 as we only apply the $L_{6 \mu\text{m}}$ -based prior on the potentially CTK sources. There are nonetheless significant differences because our updated spectral fits now yield a smaller number of CTK sources compared to L18. This is because the CTK sources in L18 deviate from the $L_X - L_{6 \mu\text{m}}$ correlations (e.g. Stern 2015) in the sense that they are systematically overluminous at X-rays for their $6 \mu\text{m}$ luminosity.

This point has been acknowledged by L18, where their CTK sources are systematically offset by more than 1σ from the Stern (2015) relationship (see fig. 4 in L18).

Table 6 is an extract of the table summarizing the results of our sample's X-ray spectral analysis after using the $L_{6 \mu\text{m}}$ -based prior. The uncertainties of the principal parameters are also indicated. For an overall summary of our sample parameter estimations, Fig. 13 displays the intrinsic X-ray luminosity (2–10 keV) as a function of the redshift and coloured as a function of the median column density.

5 OBSCURED AGN DEMOGRAPHICS

5.1 Observed parameter distribution

One of the motivations of the analysis presented in this work is to place constraints on the demographics of obscured AGN. Therefore, in the next sections, we focus on the hard-band (2–7 keV) selected sample of the *Chandra* COSMOS Legacy survey. This is because photons at rest-frame energies $>2 \text{ keV}$ can penetrate relatively dense columns of gas clouds, thereby providing a better handle on the obscured AGN population. Fig. 14 displays the LOS column density N_H distribution for all sources selected in the hard X-ray band. The histogram in this figure is constructed from the N_H posterior distributions derived by fitting the X-ray spectra of individual COSMOS sources with the baseline X-ray spectral model described in Section 3.3 and with the $L_{6 \mu\text{m}}$ -based prior (i.e. Section 4). A bootstrap resampling approach is adopted, whereby the posterior distribution of each X-ray source is resampled with replacement to generate 100 realizations of the population. These are then used to determine, within the different N_H -bins, the median fraction and 16th and 84th percentiles, corresponding to the 1σ variation lower and upper limits. Fig. 14 shows that our sample includes a large observed fraction of obscured AGN ($59.7^{+0.2}_{-0.7}$ per cent) with LOS column densities $N_H > 10^{22} \text{ cm}^{-2}$. However, the sensitivity of this survey drops close to and above the CTK limit. This is evident from the decreasing fraction of AGN in Fig. 14 towards column densities $N_H \approx 10^{24} \text{ cm}^{-2}$.

We also overplot in Fig. 14 the predictions from X-ray luminosity function (XLF) models in the literature, Ueda et al. (2014), Aird et al. (2015), and Buchner et al. (2015). The XLFs encapsulate the intrinsic number of sources as a function of their physical properties (obscuration, X-ray luminosity, and redshift). To convert these intrinsic source numbers into observed source numbers, we need to convolve them with the *Chandra* sensitivity maps. To calculate the sensitivity maps, we use the UXCLUMPY model to predict the expected *Chandra*/ACIS photon rate for an AGN of a given redshift, 2–10 keV luminosity and absorbing hydrogen column density. For the calculation of photon rates, we assume a Gaussian photon index distribution (mean 1.9, scatter 0.15) for UXCLUMPY and a soft-excess component logarithmic normalization that is uniformly distributed in the range of $10^{-7} - 10^{-1.5}$. We marginalize over these two parameters to calculate the average photon rate $\nu(z, L_X, N_H)$. This can then be converted into the area over which such a source can be detected by using the sensitivity curves derived in Section 2.1. The end products of these calculations are cubes describing the survey area available to sources as a function of L_X , z , N_H . By normalizing them, one obtains the detection probability of a source as a function of its intrinsic characteristics. Fig. 15 shows the two-dimensional projection of such a cube on the redshift-luminosity plane for a CTK source with $N_H = 1.26 \times 10^{24} \text{ cm}^{-2}$. This figure shows that the probability of detecting such a source decreases towards lower luminosities and higher redshift. The analytic XLFs are convolved

Table 6. X-ray spectral fitting results. (1) source ID; (2) redshift; (3) redshift type: spectroscopic, photometric or None; (4) X-ray 2–10 keV logarithmic luminosity and its 1σ uncertainty; (5) logarithmic column density N_{H} and its 1σ uncertainty; (6) photon index Γ and its 1σ uncertainty; (7) CTK candidate flag i.e. if the original spectroscopic fit includes more than 5 per cent of its posterior distribution in the CTK regime; (8) double-peaked flag (see definition in section 3.5); (9) source ID in the multiwavelength catalogue (Jin et al. 2018) if available; (10) logarithmic AGN $L_{6\mu\text{m}}$ from SED fitting and its 1σ uncertainty; (11) logarithmic AGN $L_{6\mu\text{m}}$ upper limit at 99 percentile if the SED fit is unconstrained. Full table electronically available.

ID	z	z type	$\log(L_X)$ (erg s^{-1})	$\log(N_{\text{H}})$ (cm^{-2})	Γ	CTK candidate	2-peaked (8)	ID Jin et al. (2018) (9)	$\log(L_{6\mu\text{m}})$ (erg s^{-1})	$L_{6\mu\text{m}}$ upp. lim (erg s^{-1})
(1)	(2)	(3)	(4)	(5)	(6)	(7)	(8)	(9)	(10)	(11)
COSMOS_0_1	1.342	zphot	$44.25^{+0.08}_{-0.11}$	$21.10^{+0.76}_{-0.76}$	$1.90^{+0.13}_{-0.13}$	False	False	–	–	–
COSMOS_0_10	1.283	zphot	$43.52^{+0.27}_{-0.25}$	$22.38^{+0.36}_{-0.82}$	$1.94^{+0.15}_{-0.14}$	False	False	10043855	–	43.82
COSMOS_0_100	0.582	zphot	$43.01^{+1.18}_{-0.70}$	$22.16^{+0.62}_{-0.31}$	$1.96^{+0.13}_{-0.15}$	False	False	10050161	$42.56^{+0.27}_{-0.19}$	–
COSMOS_0_101	0.619	zphot	$42.98^{+0.12}_{-0.14}$	$22.41^{+0.15}_{-0.19}$	$1.93^{+0.14}_{-0.15}$	False	False	10051883	–	43.14
COSMOS_0_102	0.516	zphot	$42.33^{+0.73}_{-1.17}$	$21.35^{+0.62}_{-0.90}$	$1.93^{+0.14}_{-0.16}$	False	False	–	–	–
⋮	⋮	⋮	⋮	⋮	⋮	⋮	⋮	⋮	⋮	⋮
COSMOS_8_95	2.212	zphot	$44.01^{+0.37}_{-0.93}$	$21.72^{+0.76}_{-1.01}$	$1.87^{+0.14}_{-0.13}$	False	False	10203746	–	44.29
COSMOS_8_96	0.205	zphot	$41.72^{+0.09}_{-0.10}$	$21.37^{+0.35}_{-0.56}$	$1.84^{+0.14}_{-0.13}$	True	True	10203914	$42.34^{+0.10}_{-0.09}$	–
COSMOS_8_97	1.608	zspec	$44.43^{+0.04}_{-0.05}$	$21.57^{+0.42}_{-0.85}$	$1.96^{+0.11}_{-0.11}$	False	False	10204309	$44.63^{+0.18}_{-0.17}$	–
COSMOS_8_98	2.620	zspec	$44.56^{+0.11}_{-0.09}$	$22.00^{+0.67}_{-1.26}$	$1.87^{+0.14}_{-0.14}$	False	False	–	–	–
COSMOS_8_99	0.686	zphot	$42.96^{+0.11}_{-0.15}$	$20.68^{+0.56}_{-0.48}$	$2.05^{+0.13}_{-0.15}$	False	False	20010065	$43.51^{+0.09}_{-0.08}$	–

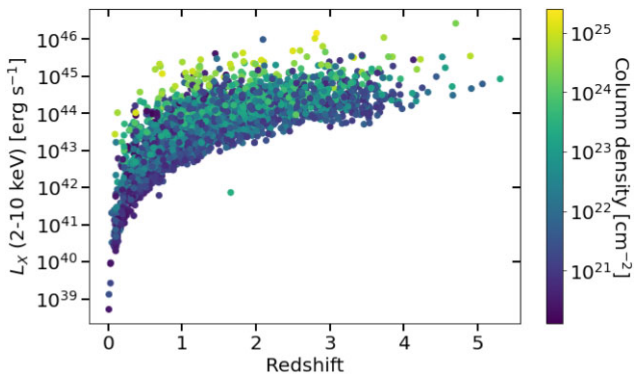


Figure 13. Intrinsic X-ray luminosity (2–10 keV) against the redshift for the sources of our sample. The colour indicates the column density of the source in cm^{-2} . The values used in this figure correspond to the median of the posterior distribution of the respective parameters. The points' locations are not very representative in the case of broad distributions, for example, in the case of the outlier source at $z \sim 1.7$ with $L_X \sim 10^{42} \text{ erg s}^{-1}$.

with the sensitivity maps and then integrated over luminosity and redshift to yield the predictions on the number of AGN as a function of N_{H} in Fig. 14.

The comparison with predictions is intended to guide the expected N_{H} distribution of AGN in the COSMOS field based on established knowledge of their demographics. We caution that comparing these model predictions and the observations should be taken with a grain of salt. This is because the histogram of the posteriors in Fig. 14 represents the convolution of the intrinsic column density distribution of AGN with the observational uncertainties. Instead, the model XLFs do not include such errors. It is nevertheless interesting that the overall shape of the model/observed column density distributions is similar. There is an increase in the number of sources with increasing column density to $\log N_{\text{H}}/\text{cm}^{-2} \approx 23.5$ followed by a steep decline for higher levels of obscuration.

Fig. 16 further explores the redshift distribution of the AGN for different N_{H} intervals. In this plot, our histograms are constructed using the same bootstrapping methodology described above. Both the

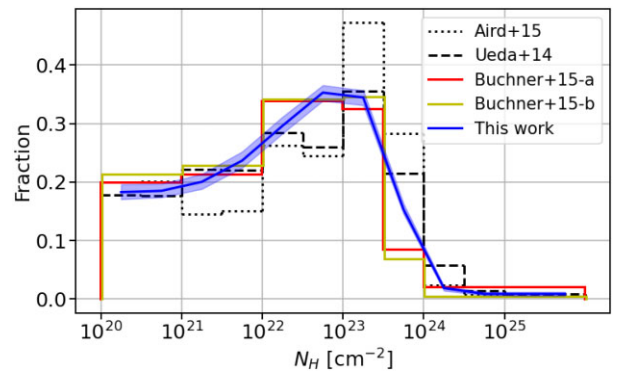


Figure 14. N_{H} distribution of the hard band detected sources in the *Chandra* COSMOS Legacy field. The thick blue line corresponds to the constraints from our X-ray spectral analysis. It represents the median of the bootstrap resampling approach described in the text. The light blue shaded region corresponds to the 68 percent confidence interval around the median. The black dotted line and the black dashed histograms show the predicted N_{H} distributions obtained, using the Aird et al. (2015) and Ueda et al. (2014) luminosity functions, respectively. The red and yellow lines represent the redshift distribution estimated in Buchner et al. (2015) obtained by using a constant-value prior and a constant-slope prior, respectively.

model and the observed distributions in Fig. 16 show a broad peak at $z \approx 1$ and a decline to higher redshift. This behaviour can be explained by the overall redshift evolution of the XLF and the flux limit of the COSMOS Legacy survey, which yields increasingly smaller AGN samples at higher redshift. This trend is broadly reproduced by the XLFs of Ueda et al. (2014), Aird et al. (2015), and Buchner et al. (2015).

5.2 Space density measurements

This section describes how the X-ray spectral analysis results are combined with the X-ray selection function of the COSMOS Legacy survey for the hard band-selected sources, to determine the space

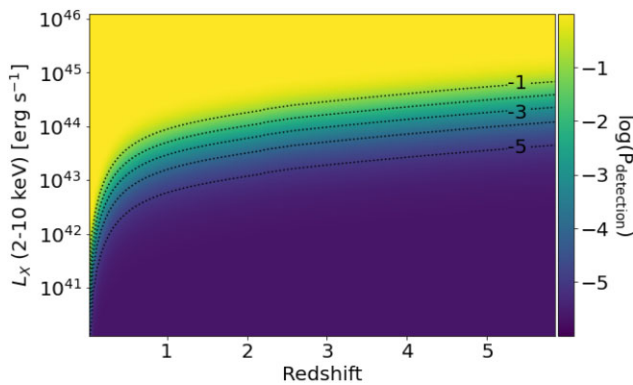


Figure 15. Sensitivity map showing the probability of detection of a CTX source with $\log(N_{\text{H}}) = 24.1 \text{ cm}^{-2}$ within *Chandra* COSMOS Legacy as a function of its intrinsic X-ray luminosity and redshift. The probability is given on a logarithmic scale. The black dotted lines indicate detection probabilities from 10^{-1} (top) to 10^{-5} (bottom) in logarithmic steps of 1 dex. As expected, the detection probability rapidly decreases with the increasing redshift and increases with the luminosity.

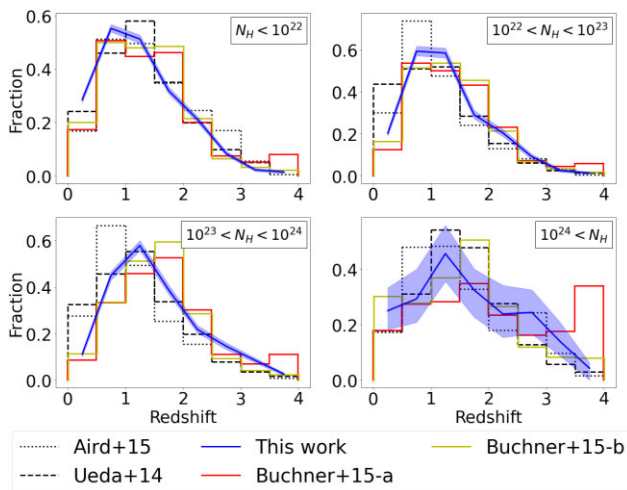


Figure 16. Redshift distributions of the hard band detected sources in the *Chandra* COSMOS Legacy field. Each panel corresponds to a different N_{H} interval. The thick blue line is the median of the bootstrap resampling approach described in the text. The light blue shaded region corresponds to the 68 per cent confidence interval around the median. When available, the redshift information comes from spectroscopy or otherwise from the redshift posterior distributions generated by the X-ray spectral fitting analysis using the photometric redshift distribution as a prior. The black dotted line and the black dashed histograms show the predicted N_{H} distributions obtained using the Aird et al. (2015) and Ueda et al. (2014) luminosity functions, respectively. The red and yellow lines represent the redshift distribution estimated in Buchner et al. (2015) obtained by using a constant-value prior and a constant-slope prior, respectively.

density of AGN as a function of the redshift z , X-ray luminosity $L_X(2 - 10 \text{ keV})$, and column density N_{H} .

Given a model of AGN space density, $\phi(L_X, z, N_{\text{H}})$, described by a set of parameters, Ψ , the likelihood of a given a set of observations, D , is described by the product of the Poisson probabilities of individual sources:

$$\mathcal{L}(D|\Psi) = e^{-\lambda} \prod_i^n \int d \log L_X \int d \log N_{\text{H}} \int \frac{dV}{dz} dz p(z, L_X, N_{\text{H}}|D_i) \phi(L_X, z, N_{\text{H}}|\Psi), \quad (7)$$

where n is the number of individual sources in the field, i is their index, $\frac{dV}{dz}$ is the differential co-moving volume. Then, $p(z, L_X, N_{\text{H}}|D_i)$ is the probability that a source has a luminosity L_X , a redshift z , and column density N_{H} . It encapsulates the uncertainty of deriving these values from the observations, i.e. from X-ray spectral analysis or in the case of photometric redshifts from the multiwavelength SED fits. The quantity λ is the expected number of AGN in the survey as a function of the parameters set and is defined as

$$\lambda = \int d \log L_X \int d \log N_{\text{H}} \int \frac{dV}{dz} dz A(z, L_X, N_{\text{H}}) \phi(L_X, z, N_{\text{H}}|\Psi), \quad (8)$$

where $A(z, L_X, N_{\text{H}})$ is the sensitivity curve representing the area of the survey for which a source with z , L_X and N_{H} can be detected and its calculation is described in Section 5.1.

We decide to use a non-parametric approach to determine the luminosity function (following Buchner et al. 2015; Georgakakis et al. 2017). The z, L_X, N_{H} parameter space is divided into a three-dimensional grid, and in each grid cell, the luminosity function is assumed to be constant. Using such a non-parametric approach allows the space density to vary more freely and eventually find large variations of shape across the parameter grid. The edges of the grid pixels in each of the three dimensions are $\log(L_X) = (40.0, 41.0, 42.0, 42.5, 43.0, 43.5, 44.0, 44.5, 45.0, 46.0, 47.0)$ [$\log(\text{erg s}^{-1})$], $z = (0.0, 0.5, 1.0, 1.5, 2.0, 2.5, 3.0, 6.0)$ and $\log(N_{\text{H}}) = (20.0, 22.0, 23.0, 24.0, 26.0)$ [$\log(\text{cm}^{-2})$]. The total number of free parameters is 280. The likelihood (equation 7) is integrated using the principle of the Importance sampling (Press et al. 1992). It is also worth emphasizing that in the Bayesian framework of equation (7) the posterior distribution $p(z, L_X, N_{\text{H}}|D_i)$ of a given source (i.e. contours and shaded regions in Figs 6 and 11) is weighted by the luminosity function $\phi(L_X, z, N_{\text{H}})$ when estimating the likelihood. Non-physical posterior solutions, e.g. very high AGN luminosities, can therefore be weighted down a posteriori because they are rare. This is the case of parametric XLF studies that typically assume a double power-law form with a relatively steep bright-end slope. In our non-parametric approach, however, there is no imposed shape, and the AGN space density at each grid point is independently determined. In that respect, our analysis is more sensitive to broad $p(z, L_X, N_{\text{H}}|D_i)$ posteriors like those shown in Fig. 6. We nevertheless compensate for that using the multiwavelength priors described in Section 4 to narrow down the X-ray spectral analysis posteriors of the sample sources.

We use STAN, a Hamiltonian Markov chain Monte Carlo code (Carpenter et al. 2017) to sample the likelihood (equation 7) in a Bayesian framework and to obtain the space density posterior distribution for each cell of the three-dimensional parameter grid. The resulting space density measurements are displayed in Fig. 17 and compared with different XLFs in the literature. We limit this comparison to $z < 2$, where the COSMOS Legacy survey provides strong constraints. At higher redshift, the number of X-ray AGN in our sample decreases rapidly, and our space density measurements suffer larger uncertainties.

Our space density measurements have a broad overall agreement with previous studies. In detail, however, there are subtle differences. For example, in the case of unobscured AGN, $N_{\text{H}} < 10^{22} \text{ cm}^{-2}$, our constraints lie systematically lower than the analytic XLFs of Ueda et al. (2014) and Aird et al. (2015), particularly for luminosities $L_X(2-10 \text{ keV}) \approx 10^{43}-10^{44} \text{ erg s}^{-1}$. This trend is stronger for the redshift intervals $z = 0.5-1$ and $1-1.5$ but is also evident in other redshift bins. For moderately obscured AGN in the range $N_{\text{H}} = 10^{22}-10^{23} \text{ cm}^{-2}$, our measurements are instead systematically higher than those of the analytic XLFs of Ueda et al. (2014) and

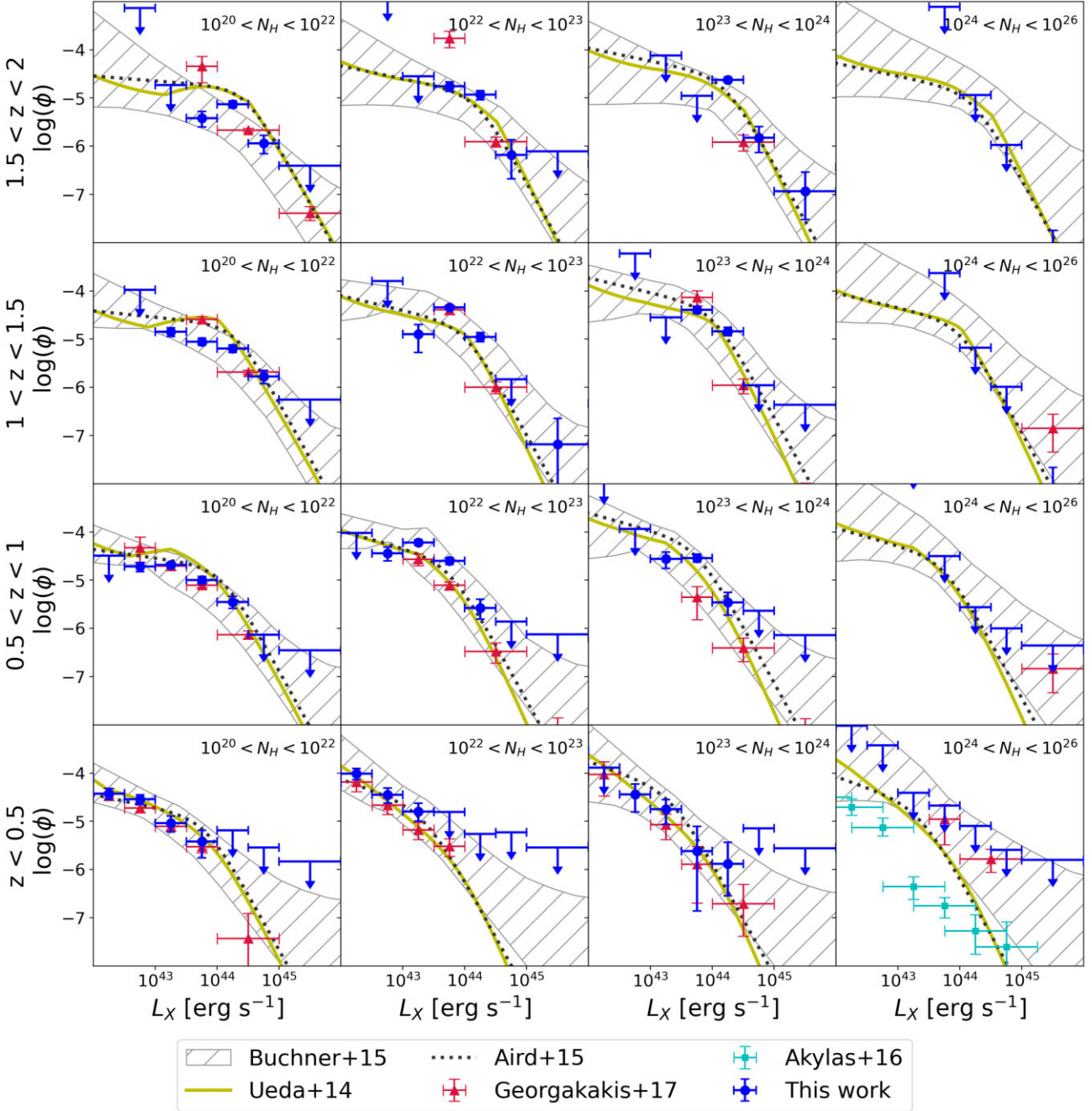


Figure 17. Space density curves ($\text{Mpc}^{-3} \text{dex}^{-2}$) as a function of the intrinsic X-ray luminosity in the 2–10 keV band for different redshift and column density intervals. The redshift range of each panel row is indicated on its left side. From top to bottom, the rows correspond to $z = 1.5-2$, $z = 1-1.5$, $z = 0.5-1$, and $z = 0-0.5$. The column density increases from left to right, as indicated at the bottom of each column. The constraints from our analysis are shown with the blue dots and associated with 1σ uncertainties and, in the case of the upper limits, with the blue arrows pointing down. A space density is considered an upper limit if its 1σ uncertainty width is larger than 2 dex. These upper limits correspond to the 3σ confidence interval. The yellow solid line and the black dotted line correspond to Ueda et al. (2014) and Aird et al. (2015) luminosity functions, respectively. The grey hatched area represents the non-parametric constraints of Buchner et al. (2015). The red triangles are the luminosity function measured by Georgakakis et al. (2017) in the XMM-XXL field (Pierre et al. 2016). The CTK luminosity function determined by Akylas et al. (2016) in the local Universe is shown with the cyan squares.

Aird et al. (2015). These differences are partly related to the fact that the NH constraints in these studies are largely based on hardness ratios, which have limited discriminating power for AGN close to the 10^{22} cm^{-2} limit. It is nevertheless reassuring that for the integrated space densities in the interval $N_{\text{H}} = 10^{20}-10^{23} \text{ cm}^{-2}$, the agreement between our analysis and the analytic studies above is

good. In any case, these differences also highlight the importance of fully non-parametric XLF approaches, like the one presented here, to supplement and guide analytic prescriptions. In the CTK regime, our analysis only yields upper limits in the AGN space density because of the low number of CTK sources in our sample. Nevertheless, the 3σ upper limits, particularly at $z > 0.5$, favour CTK space densities

at the low-end of the range covered by the previous observational constraints shown in Fig. 17.

5.3 Compton-Thick fraction

The intrinsic CTK fraction, f_{CTK} , is an important parameter for characterizing the demographics of heavily obscured AGN. In our analysis, this is defined as the ratio between the number of AGN with column density $N_{\text{H}} = 10^{24}\text{--}10^{26} \text{ cm}^{-2}$ and those with $N_{\text{H}} = 10^{20}\text{--}10^{26} \text{ cm}^{-2}$:

$$f_{\text{CTK}} = \frac{N_{24-26}}{N_{20-22} + N_{22-23} + N_{23-24} + N_{24-26}}. \quad (9)$$

In the equation above, N refers to the intrinsic number of AGN at different logarithmic column density intervals. For the estimation of f_{CTK} , we slightly modify the XLF model used in the Bayesian inference methodology. The space density of CTK AGN at all redshift and luminosity intervals is linked to that of CTN AGN via equation (9) where f_{CTK} is a free parameter of the model. After some algebra, the CTK space density is estimated as

$$\phi(L_X, z, \log N_{\text{H}} = 24\text{--}26) = \frac{f_{\text{CTK}}}{2 \cdot (1 - f_{\text{CTK}})} \cdot \left(2 \cdot \phi(L_X, z, \log N_{\text{H}} = 20\text{--}22) + \phi(L_X, z, \log N_{\text{H}} = 22\text{--}23) + \phi(L_X, z, \log N_{\text{H}} = 23\text{--}24) \right). \quad (10)$$

The multiplicative factors of 2 in the above equation account for broader logarithmic column density intervals for CTK ($\log N_{\text{H}}/\text{cm}^{-2} = 24\text{--}26$) and unobscured ($\log N_{\text{H}}/\text{cm}^{-2} = 20\text{--}22$) AGN. The f_{CTK} is assumed here to depend only on the redshift but not on the luminosity. This is equivalent to assuming that at fixed redshift, the CTK luminosity function is related to the CTN one via a scaling factor (e.g. Aird et al. 2015). The f_{CTK} parameter is therefore independently determined for each of the redshift intervals adopted in Section 5.2 with edges $z = (0.0, 0.5, 1.0, 1.5, 2.0, 2.5, 3.0, 6.0)$. The STAN Hamiltonian Markov chain Monte Carlo code then yields a posterior distribution of the f_{CTK} for each of the redshift intervals above.

Fig. 18 plots the f_{CTK} inferred from our analysis as a function of redshift for the hard band selected AGN. This parameter is constrained to be $21.0_{-9.9}^{+16.1}$ per cent (1σ) for the lowest redshift interval $z = 0\text{--}0.5$. At higher redshifts, only upper limits to f_{CTK} can be derived. Also shown in Fig. 18 are previous results on the CTK fraction that demonstrate the range of values covered by different studies. At $z = 0\text{--}0.5$, our analysis favours CTK fractions at the low end of the distribution of f_{CTK} in the literature. At higher redshift, our 3σ upper limits are generous, but at least for $z \lesssim 2$, suggest $f_{\text{CTK}} \lesssim 40$ per cent.

6 DISCUSSION

6.1 Obscuration characterization

A multiwavelength Bayesian approach is presented that combines X-ray spectral fits with information from mid-IR wavelengths to constrain the level of LOS obscuration of AGN. This is motivated by the need to resolve degeneracies between two key physical parameters inferred from X-ray spectral analysis, the intrinsic AGN luminosity and the LOS hydrogen column density. These covariances

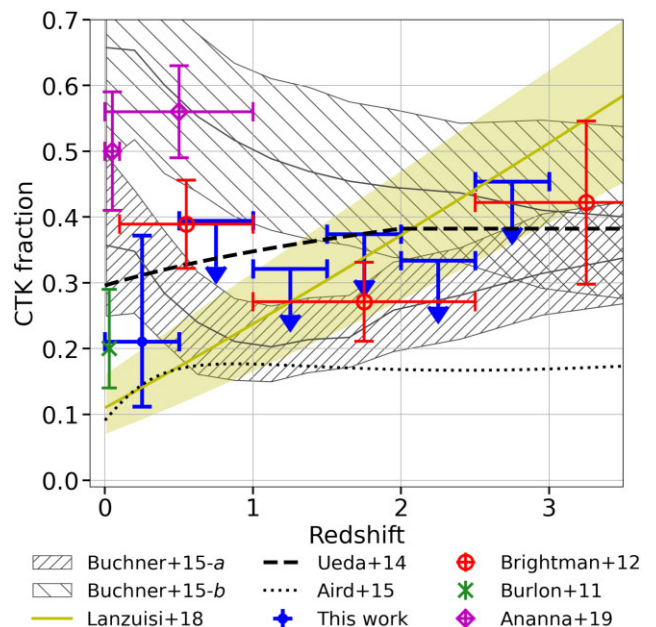


Figure 18. Intrinsic CTK fraction as a function of redshift. The blue symbols show the results of our analysis. The constraints for the redshift interval $z = 0\text{--}0.5$ (blue circle) show the mode of the posterior distribution and the associated 68 per cent confidence interval. At higher redshift intervals, the downward blue arrows correspond to the 3σ upper limit estimated from the corresponding posterior distributions. The horizontal error bars of all blue symbols show the width of the redshift intervals. The vertically (Buchner+15-a) and horizontally (Buchner+15-b) hatched shaded regions represent the 1σ uncertainty of the CTK fractions presented in Buchner et al. (2015) obtained by using a constant-value prior and a constant-slope prior, respectively. The solid line within these regions corresponds to the median. The CTK fraction of the Ueda et al. (2014) and Aird et al. (2015) XLFs are shown with the black dashed and the black dotted lines, respectively. The green cross at $z \approx 0$ is the measured CTK fraction in the local Universe determined by Burlon et al. (2011). The red circles are the results of Brightman & Ueda (2012). The yellow shaded region is the CTK fraction estimation by L18. The pink diamonds correspond to the CTK fraction estimated by Ananna et al. (2019) at redshift $z < 0.1$ and $z < 1.0$.

are particularly important for sources with a low number of counts and high levels of obscurations leading to broad or multimodal posterior distributions. Our methodology addresses this issue by using the mid-IR part of the SED as a prior for the intrinsic AGN luminosity. This is based on the expectation that the short wavelength (X-rays, UV) AGN radiation absorbed by dust and gas clouds emerges as thermal emission in the IR. Support for such an energy balance between different parts of the SED is coming from observed correlations between the intrinsic (i.e. corrected for obscuration) X-ray luminosity and the mid-IR luminosity of AGN (Gandhi et al. 2009; Stern 2015). These correlations are claimed to apply to AGN over a broad range of LOS obscurations, including CTK sources (Gandhi et al. 2009; Asmus et al. 2015; Annuar et al. 2017). Therefore, our methodology relies on such relations as an independent handle on the intrinsic accretion luminosity, particularly in the case of obscured systems. We caution, however, that in the local Universe, there are (few) examples of heavily obscured (CTK) AGN that appear subdominant in the mid-IR for their intrinsic X-ray luminosity (Krabbe, Böker & Maiolino 2001; Gandhi et al. 2015) and, therefore, deviate from the established correlations. For these sources, the mid-IR photons may be absorbed by the obscuring medium. Our methodology is not optimal for this class of AGN.

We apply our approach to X-ray sources in the *Chandra* COSMOS Legacy survey to constrain in a non-parametric way the space density of AGN in bins of luminosity, redshift and column density. We find small systematic differences between our results and previous parametric estimates of the AGN XLF in the case of unobscured ($N_{\text{H}} < 10^{22} \text{ cm}^{-2}$) and moderately obscured ($N_{\text{H}} = 10^{22} - 10^{23} \text{ cm}^{-2}$) systems. This highlights the importance of further work to better constrain the column density distribution of AGN. Additionally, the *eROSITA* (Predehl et al. 2021) surveys have the potential to address this issue by providing large numbers of moderately obscured AGN out to high redshift and higher L_X .

At higher but still CTN levels of obscuration ($N_{\text{H}} = 10^{23} - 10^{24} \text{ cm}^{-2}$), our measurements are in fair agreement with previous analytic XLF determinations within the uncertainties of the individual data points. For CTK column densities, our analysis yields only upper limits to the space density. It is nevertheless interesting that for redshifts $z > 0.5$ and luminosities $L_X \approx 10^{44} - 10^{45} \text{ erg s}^{-1}$, the 3σ upper limits overlap with the Ueda et al. (2014) and Aird et al. (2015) XLFs and therefore provide informative constraints on the space density of AGN with $N_{\text{H}} > 10^{24} \text{ cm}^{-2}$.

An alternative approach for quantifying the CTK AGN demographics is via their fraction relative to the overall AGN population (see equation 9). Fig. 18 shows previous estimates of this fraction in comparison with our constraints. At low redshift, $z < 0.5$, our results favour low CTK fractions, although the uncertainties remain large, $f_{\text{CTK}} = 21.0_{-9.9}^{+16.1}$ per cent. Burlon et al. (2011) used the 3-yr *Swift*-BAT (Burst Alert Telescope; Barthelmy et al. 2005) serendipitous survey to measure a CTK fraction of about 20 per cent in the local Universe. Their sample is selected at hard energies (14–195 keV) and is, therefore, least biased by obscuration effects. Low CTK fractions in the range $f_{\text{CTK}} \approx 10$ –20 per cent are also proposed by Akylas et al. (2016) and Georgantopoulos & Akylas (2019) based on AGN selected from the 70-month *Swift*-BAT survey. These authors also emphasise the importance of the assumptions on the shape of the CTK AGN X-ray spectrum (e.g. the strength of reflection relative to the direct component, high-energy cut-off) for interpreting the high energy spectra of AGN and deriving CTK fractions.

Buchner et al. (2015) analysed the X-ray spectrum of AGN detected in popular extra-galactic survey fields. They constrained the AGN space density using a non-parametric approach, similar to that presented here, but also imposing two different continuity priors. They tend to keep either the value or the slope of the XLF constant in areas of the parameter space with few data to provide meaningful constraints. Fig. 18 shows the CTK fraction of each of these two priors. These are estimated by marginalizing the Buchner et al. (2015) posteriors in the luminosity interval $10^{42} - 10^{46} \text{ erg s}^{-1}$. At low redshift, $z < 0.5$, our results are lower but still marginally consistent with the constant-value prior estimates of Buchner et al. (2015).

At higher redshift, $z > 0.5$, our 3σ upper limits also favour the constant-value prior estimates of Buchner et al. (2015), at least up to $z \approx 2.5$. These upper limits are also broadly consistent with the constraints presented by Brightman & Ueda (2012) and also track the f_{CTK} redshift evolution inferred by L18. We caution that the latter observational constraint corresponds to a luminosity of $L_X(2-10 \text{ keV}) = 10^{45} \text{ erg s}^{-1}$ at all redshifts. It is also worth noting that the difference between the Ueda et al. (2014) and Aird et al. (2015) curves in Fig. 18 is because of differences in the space density of CTN AGN ($N_{\text{H}} = 10^{22} - 10^{24} \text{ cm}^{-2}$). This is also evident by the somewhat higher normalization of the Aird et al. (2015) XLF relative to that Ueda et al. (2014) in the two middle rows of panels in Fig. 17.

In Fig. 18, there is a disagreement between our results and the recent estimates of the CTK fraction of Ananna et al. (2019). They developed an AGN population synthesis model that fits observations of the diffuse X-ray background spectrum using as input the XLF and models for the X-ray spectra of AGN. Their best-fitting model predicts CTK AGN fractions of 50 ± 9 per cent at $z \approx 0.1$, which is higher than our estimates, but also other studies that use spectral analysis of X-ray selected samples to infer CTK fractions directly (e.g. Ricci et al. 2015). We caution that models of the diffuse X-ray background spectrum suffer strong degeneracies between the adopted shape of the X-ray spectra of AGN (i.e. strength of the reflection component, power-law index) and the assumed CTK fraction (Treister, Urry & Virani 2009). Akylas et al. (2012), for example, showed that low CTK fractions could be compensated by a stronger X-ray reflection component (and vice versa) to yield diffuse X-ray background spectra consistent with observations.

The inferred CTK fractions also have implications on fundamental properties of the accretion flow on to SMBHs, such as the radiative efficiency, ϵ . Shankar et al. (2020) developed models that allow the determination of this parameter based on the observed population properties of AGN samples. They argue in particular that observational measurements of the mean X-ray luminosity averaged over galaxy populations as a function of stellar mass (e.g. Yang et al. 2017) provide interesting constraints to ϵ . Their analysis suggests $\epsilon \gtrsim 0.15$ for the black-hole mass versus stellar mass relation of Shankar et al. (2016), in line with theoretical expectations. A significant source of uncertainty in this analysis is the fraction of heavily obscured and CTK AGN that may be underrepresented in X-ray-selected samples because of their apparent faintness. If there is a large population of such missing sources, then observational measurements of the mean X-ray luminosity as a function of stellar mass are biased, now leading to the underestimation of the AGN radiative efficiency. Our findings for moderate fractions of Compton thick AGN, at least at $z \approx 0.1$, suggest that such an effect is small and hence has a minor effect on the inferred ϵ values.

Additionally, within the context of AGN/galaxy co-evolution scenarios, there are suggestions that heavily obscured AGN represent an important early stage of black-hole growth (e.g. Hopkins et al. 2008). They are systems observed close to the peak of their nuclear (and star formation) activity, at a stage just before the AGN winds blow away the obscuring dust and gas clouds and eventually quench the star formation in the host galaxy. The low fractions of Compton thick AGN estimated in our work have implications for the duty cycle of the obscured phase of the scenario above. Additionally, our proposed methodology can help isolate reliable samples of heavily obscured and CTK AGN to test the co-evolution scenario above by studying the properties of their host galaxies relative to less obscured sources.

6.2 Future missions

One of the core science objectives of the *Athena* X-ray observatory (Nandra et al. 2013) is the characterization of the demographics of heavily obscured and CTK AGN out to high redshift, $z \approx 4$ (Georgakakis et al. 2013). The means to achieve this goal are multitiered surveys with the Wide Field Imager (WFI; Rau et al. 2013) onboard the *Athena* X-ray observatory. The larger collecting area of *Athena* in the energy range of 0.5–10 keV (2500 cm² at 6 keV) compared to e.g. *Chandra*, 28 cm² at 6.5 keV, or *XMM-Newton*, 900 cm² at 7 keV, translates into a significant improvement in X-ray spectral quality and ability to identify and characterize the intrinsic properties of heavily obscured and CTK sources.

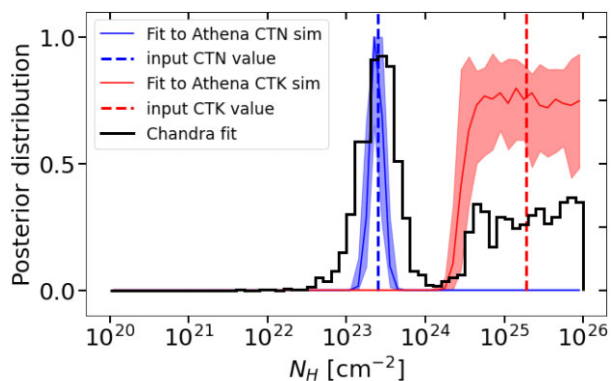


Figure 19. The black histogram shows the N_{H} posterior distribution of the X-ray spectroscopic fit of *Chandra* COSMOS.1_420 without using prior. From the CTN peak (CTK peak, respectively), we simulate an *Athena*/WFI source at $z = 1.55$ with $N_{\text{H}} = 2.51 \times 10^{23} \text{ cm}^{-2}$ and $L_{\text{X}} = 1.07 \times 10^{44} \text{ erg s}^{-1}$ ($N_{\text{H}} = 1.86 \times 10^{25} \text{ cm}^{-2}$, $L_{\text{X}} = 2.09 \times 10^{45} \text{ erg s}^{-1}$, respectively). The spectroscopic N_{H} posterior distribution of these simulations are represented in blue (red, respectively). The vertical dashed lines correspond to the input N_{H} values for the respective simulations.

We demonstrate this capacity using one of the *Chandra* COSMOS Legacy sources with bimodal column density distribution that includes both CTK and CTN sources. The source ID is COSMOS.1_420, with a spectroscopic redshift of 1.55. Fig. 19 shows the posterior distribution of that source using the *Chandra* COSMOS Legacy observations without applying a $L_{6\mu\text{m}}$ prior. It also displays the most likely CTK and CTN solutions which are ($N_{\text{H}} = 1.86 \times 10^{25} \text{ cm}^{-2}$, $L_{\text{X}} = 2.09 \times 10^{45} \text{ erg s}^{-1}$) and ($N_{\text{H}} = 2.51 \times 10^{23} \text{ cm}^{-2}$, $L_{\text{X}} = 1.07 \times 10^{44} \text{ erg s}^{-1}$), respectively. We then use the current *Athena* calibration files² to independently simulate the X-ray spectra of both solutions with the UXCLUMPY model.

In this exercise, we adopt an exposure time of 100 ks that approximately corresponds to the wide-area tile of the *Athena*/WFI survey plan. The adopted background model is an updated version of the WFI background file generation model.³ We assume an extraction aperture of 5 arcsec that corresponds to an EEf of ~ 69 per cent for the FOV-average *Athena* PSF. The same model is then used with BXA to refit the simulated spectra. The resulting posteriors are also shown in Fig. 19. It is clear that for luminous X-ray sources like the COSMOS.1_420 example, X-ray spectroscopy with the *Athena*/WFI alone is sufficient to yield unimodal posteriors and distinguish between CTK and CTN solutions.

Nevertheless, the *Athena*/WFI surveys will also be sensitive to heavily obscured AGN of lower luminosity. We therefore repeat the analysis by renormalizing the X-ray luminosity of the CTN solution of the source COSMOS.1_420 to $L_{\text{X}}(2-10 \text{ keV}) = 10^{43} \text{ erg s}^{-1}$ (~ 10 times fainter) and the CTK solution to $L_{\text{X}}(2-10 \text{ keV}) = 10^{44} \text{ erg s}^{-1}$ (~ 20 times fainter). The resulting posteriors for different exposure times are shown in Fig. 20. Short exposure times result in low photon counts leading to broader column density probability distributions that make the determination of the CTK nature of the source uncertain. For instance, with 100 ks exposure time, the fits of the simulation from the CTN and CTK solutions have, respectively, 46 and 57 per cent of their posterior distribution in the CTK regime. In this example, the obscuration regime of the source is highly uncertain.

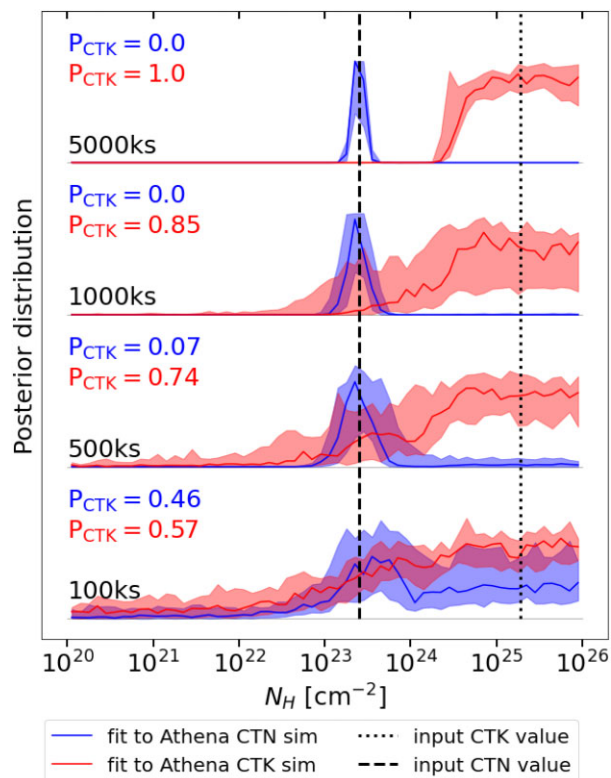


Figure 20. Column density posterior distribution of the X-ray spectroscopic fit for the CTN (blue) and CTK (red) *Athena*/WFI simulations of COSMOS.1_420 at $z = 1.55$. The intrinsic X-ray luminosity are renormalized at $L_{\text{X}}(2-10 \text{ keV}) = 10^{43} \text{ erg s}^{-1}$ and at $L_{\text{X}}(2-10 \text{ keV}) = 10^{44} \text{ erg s}^{-1}$ for the CTN and CTK solutions, respectively. The distributions are shifted as a function of their exposure time for *Athena*/WFI: 100, 500, 1000, and 5000 ks. The dashed vertical line represents the CTN input column density at $N_{\text{H}} = 2.51 \times 10^{23} \text{ cm}^{-2}$, and the dotted vertical line represents the CTK input column density at $N_{\text{H}} = 1.86 \times 10^{25} \text{ cm}^{-2}$. P_{CTK} , the fraction of the posterior distribution in the CTK regime, is indicated for each exposure time and for both the CTN and CTK *Athena* simulation with their respective colour.

The posterior broadening can be compensated by a higher exposure time (e.g. $\gtrsim 1000$ ks for the CTN source or $\gtrsim 5000$ ks for the CTK source). It significantly increases the contrast between the posterior distributions from the two simulations. However, such large exposure time are unrealistic for large surveys as planned for *Athena*. Alternatively, the methodology based on mid-IR priors proposed in this paper could narrow down the posteriors and guarantee the obscuration regime of the source. Doing so would improve the *Athena* constraints on AGN demographics.

In addition to the *Athena* observatory, observations by the *James Webb Space Telescope* (Gardner et al. 2006) will improve SED constraints and allow a better understanding of the correlation between X-rays and the mid-IR, on which our methodology hinges. The Euclid survey (Laureijs et al. 2011) will also provide improved photometric redshifts over large areas of the sky, particularly for the obscured AGN population, for which the optical bands are dominated by stellar light of the galaxy.

7 SUMMARY

To understand the growth of SMBH throughout the Universe, one has to get a complete census of AGN and efficiently constrain their physical parameters. This paper proposes a new methodology to

²https://www.mpe.mpg.de/ATHENA-WFI/response_matrices.html

³WFI-MPE-ANA-0010_i7.1_Preparation-of-Background-Files.pdf

extract the properties of X-ray selected AGNs within the *Chandra* COSMOS Legacy survey containing 2965 sources (Section 2). To our knowledge, this is the first time that these observations have been used to constrain the AGN XLF. The novelty of our analysis is the inclusion of mid-IR priors in the Bayesian-based X-ray spectral analysis (Section 4). With SED fitting, we constrain the luminosity of the AGNs at $6\ \mu\text{m}$ that is later used as a proxy for the accretion X-ray luminosity guiding the X-ray spectroscopy. This approach improves the confidence of the constraints on physical parameters by breaking down degeneracies, such as between X-ray luminosity and LOS hydrogen column density. This approach primarily benefits the low photon statistics and the most heavily obscured sources. By carefully considering the X-ray selection function, we measure the AGN space density as a function of the accretion X-ray luminosity, LOS obscuration and redshift. We also estimate the CTK fraction as a function of the redshift (Section 5). The main results of our new analysis are as follows:

(i) Our AGN space density measurements are in broad agreement with previous analytic studies. As we find a small number of CTK AGN (27 sources) in the *Chandra* COSMOS Legacy field, we can only place upper limits on the space density of this population (Section 5.2).

(ii) Our CTK fractions estimation are at the low end of the range determined in previous studies. At redshift $z < 0.5$, we find $f_{\text{CTK}} = 21.0_{-9.9}^{+16.1}$ per cent. At $0.5 < z < 2.5$, we determine (3σ) upper limits that suggest a CTK fraction typically lower than 40 per cent, lower than several previous studies (Section 5.3).

(iii) By simulating spectra, we found that future missions like the *Athena* observatory would benefit from this multiwavelength methodology to better constrain the physical parameters of the faintest and most obscured sources (Section 6.2).

The multiwavelength-based methodology proposed in this paper efficiently increases the confidence of obscuration measurements and AGN demographics. Our results can be used in various fields of SMBH research like their growth, their evolution through time or the AGN co-evolution with the host-galaxy.

ACKNOWLEDGEMENTS

We thank the anonymous referee for their comments and suggestions. This work has been supported by the EU H2020-MSCA-ITN-2019 Project 860744 ‘BiD4BEST: Big Data applications for black hole Evolution Studies.’ This research made use of ASTROPY,⁴ a community-developed core PYTHON package for Astronomy (Astropy Collaboration 2013, 2018). This research has made use of data obtained from the Chandra Data Archive and the Chandra Source Catalog, and software provided by the Chandra X-ray Center (CXC) in the application packages CIAO and SHERPA. For analysing X-ray spectra, we use the analysis software BXA (Buchner et al. 2014), which connects the nested sampling algorithm ULTRANEST (Buchner 2021) with the fitting environment CIAO/SHERPA (Fruscione et al. 2006).

DMA and DJR acknowledges the Science Technology and Facilities Council (STFC) for support through grant no. ST/T000244/1.

JA acknowledges support from a UKRI Future Leaders Fellowship (grant no. MR/T020989/1).

FJC acknowledges financial support from the Spanish Ministry MCIU under project RTI2018-096686-B-C21

⁴<http://www.astropy.org>

(MCIU/AEI/FEDER/UE), cofunded by FEDER funds and from the Agencia Estatal de Investigación, Unidad de Excelencia María de Maeztu, ref. MDM-2017-0765.

AL is partly supported by the PRIN MIUR 2017 prot. 20173ML3WW 002 ‘Opening the ALMA window on the cosmic evolution of gas, stars, and massive black holes’.

CRA acknowledges support from the projects ‘Feeding and feedback in active galaxies’, with reference PID2019-106027GB-C42, funded by MICINN-AEI/10.13039/501100011033, ‘Quantifying the impact of quasar feedback on galaxy evolution’, with reference EUR2020-112266, funded by MICINN-AEI/10.13039/501100011033 and the European Union NextGenerationEU/PRTR, and from the Consejería de Economía, Conocimiento y Empleo del Gobierno de Canarias and the European Regional Development Fund (ERDF) under grant ‘Quasar feedback and molecular gas reservoirs’, with reference ProID2020010105, AC-CISI/FEDER, UE.

For the purpose of open access, the authors have applied a Creative Commons Attribution (CC BY) licence to any Author Accepted Manuscript version arising from this submission.

DATA AVAILABILITY

We release two tables containing information on the sources of our sample. The first one contains the information relative to the spectral extraction and is partially displayed in Table 2. The second one contains the results of the fit by BXA and is partially displayed in Table 6. We also release the STAN products for the space density and CTK fraction calculations. The files are described and available at <https://doi.org/10.5281/zenodo.7014625>.

All other data products used in this paper are available on-demand to the authors.

REFERENCES

- Aird J., Coil A. L., Georgakakis A., 2017, *MNRAS*, 465, 3390
 Aird J., Coil A. L., Georgakakis A., 2018, *MNRAS*, 474, 1225
 Aird J., Coil A. L., Georgakakis A., 2019, *MNRAS*, 484, 4360
 Aird J., Coil A. L., Georgakakis A., Nandra K., Barro G., Pérez-González P. G., 2015, *MNRAS*, 451, 1892
 Akylas A., Georgakakis A., Georgantopoulos I., Brightman M., Nandra K., 2012, *A&A*, 546, A98
 Akylas A., Georgantopoulos I., Ranalli P., Gkiokas E., Corral A., Lanzuisi G., 2016, *A&A*, 594, A73
 Alexander D. M. et al., 2008, *ApJ*, 687, 835
 Alexander D. M. et al., 2013, *ApJ*, 773, 125
 Alexander D. M., Hickox R. C., 2012, *New Astron. Rev.*, 56, 93
 Ananna T. T. et al., 2019, *ApJ*, 871, 240
 Andonie C. et al., 2022, *MNRAS*, 517, 2577
 Annuar A. et al., 2017, *ApJ*, 836, 165
 Antonucci R., 1993, *ARA&A*, 31, 473
 Asmus D., Gandhi P., Hönig S. F., Smette A., Duschl W. J., 2015, *MNRAS*, 454, 766
 Assef R. J. et al., 2015, *ApJ*, 804, 27
 Assef R. J., Stern D., Noirot G., Jun H. D., Cutri R. M., Eisenhardt P. R. M., 2018, *ApJS*, 234, 23
 Astropy Collaboration, 2013, *A&A*, 558, A33
 Astropy Collaboration, 2018, *AJ*, 156, 123
 Barger A. J. et al., 2003, *AJ*, 126, 632
 Barthelmy S. D. et al., 2005, *Space Sci. Rev.*, 120, 143
 Bianchi S., Guainazzi M., Chiaberge M., 2006, *A&A*, 448, 499
 Brightman M., Nandra K., 2011, *MNRAS*, 414, 3084
 Brightman M., Ueda Y., 2012, *MNRAS*, 423, 702
 Brusa M. et al., 2007, *ApJS*, 172, 353

- Bruzual G., Charlot S., 2003, *MNRAS*, 344, 1000
- Buchner J. et al., 2014, *A&A*, 564, A125
- Buchner J. et al., 2015, *ApJ*, 802, 89
- Buchner J., 2016, *Statistics and Computing*, 26, 383
- Buchner J., 2019, *PASP*, 131, 108005
- Buchner J., 2021, *J. Open Source Softw.*, 6, 3001
- Buchner J., Brightman M., Nandra K., Nikutta R., Bauer F. E., 2019, *A&A*, 629, A16
- Burlon D., Ajello M., Greiner J., Comastri A., Merloni A., Gehrels N., 2011, *ApJ*, 728, 58
- Capak P. et al., 2007, *ApJS*, 172, 99
- Carpenter B. et al., 2017, *J. Stat. Softw.*, 76, 1
- Cash W., 1979, *ApJ*, 228, 939
- Chen C.-T. J. et al., 2017, *ApJ*, 837, 145
- Civano F. et al., 2016, *ApJ*, 819, 62
- Dale D. A., Helou G., Magdis G. E., Armus L., Díaz-Santos T., Shi Y., 2014, *ApJ*, 784, 83
- Del Moro A. et al., 2016, *MNRAS*, 456, 2105
- Della Ceca R. et al., 2008, *A&A*, 487, 119
- Delvecchio I. et al., 2014, *MNRAS*, 439, 2736
- Donley J. L. et al., 2012, *ApJ*, 748, 142
- Elvis M. et al., 2009, *ApJS*, 184, 158
- Elvis M., 2000, *ApJ*, 545, 63
- Fernique P., Boch T., Donaldson T., Durand D., O’Mullane W., Reinecke M., Taylor M., 2019, MOC - HEALPix Multi-Order Coverage map Version 1.1, IVOA Recommendation 07 October 2019.
- Fruscione A. et al., 2006, in Silva D. R., Doxsey R. E., eds, *SPIE Astronomical Telescopes + Instrumentation*. SPIE, Bellingham, p. 62701V
- Gandhi P., Horst H., Smette A., Hönlig S., Comastri A., Gilli R., Vignali C., Duschl W., 2009, *A&A*, 502, 457
- Gandhi P., Yamada S., Ricci C., Asmus D., Mushotzky R. F., Ueda Y., Terashima Y., La Parola V., 2015, *MNRAS*, 449, 1845
- Gardner J. P. et al., 2006, *Space Sci. Rev.*, 123, 485
- Georgakakis A. et al., 2013, preprint ([arXiv:1306.2328](https://arxiv.org/abs/1306.2328))
- Georgakakis A., Aird J., Schulze A., Dwelly T., Salvato M., Nandra K., Merloni A., Schneider D. P., 2017, *MNRAS*, 471, 1976
- Georgakakis A., Nandra K., Laird E. S., Aird J., Trichas M., 2008, *MNRAS*, 388, 1205
- Georgantopoulos I. et al., 2011, *A&A*, 534, A23
- Georgantopoulos I., Akylas A., 2019, *A&A*, 621, A28
- Gilli R., Comastri A., Hasinger G., 2007, *A&A*, 463, 79
- Górski K. M., Hivon E., Banday A. J., Wandelt B. D., Hansen F. K., Reinecke M., Bartelmann M., 2005, *ApJ*, 622, 759
- Griffin M. J. et al., 2010, *A&A*, 518, L3
- Hickox R. C., Alexander D. M., 2018, *ARA&A*, 56, 625
- Hopkins P. F., Hernquist L., Cox T. J., Kereš D., 2008, *ApJS*, 175, 356
- Jeffreys H., 1961, *Theory of Probability*, 3rd edn. Oxford Univ. Press, New York
- Jin S. et al., 2018, *ApJ*, 864, 56
- Kalberla P. M. W., Burton W. B., Hartmann D., Arnal E. M., Bajaja E., Morras R., Pöppel W. G. L., 2005, *A&A*, 440, 775
- Kormendy J., Ho L. C., 2013, *ARA&A*, 51, 511
- Krabbe A., Böker T., Maiolino R., 2001, *ApJ*, 557, 626
- Laird E. S. et al., 2009, *ApJS*, 180, 102
- Lanzuisi G. et al., 2018, *MNRAS*, 480, 2578
- Laureijs R. et al., 2011, preprint ([arXiv:1110.3193](https://arxiv.org/abs/1110.3193))
- Le Floch E. et al., 2009, *ApJ*, 703, 222
- Levenson N. A., Heckman T. M., Krolik J. H., Weaver K. A., Życki T. P., 2006, *ApJ*, 648, 111
- Lutz D. et al., 2011, *A&A*, 532, A90
- Maiolino R., Salvati M., Bassani L., Dadina M., della Ceca R., Matt G., Risaliti G., Zamorani G., 1998, *A&A*, 338, 781
- Marchesi S. et al., 2016a, *ApJ*, 817, 34
- Marchesi S. et al., 2016b, *ApJ*, 830, 100
- Marconi A., Risaliti G., Gilli R., Hunt L. K., Maiolino R., Salvati M., 2004, *MNRAS*, 351, 169
- Markowitz A. G., Krumpe M., Nikutta R., 2014, *MNRAS*, 439, 1403
- Mateos S. et al., 2012, *MNRAS*, 426, 3271
- Mateos S. et al., 2015, *MNRAS*, 449, 1422
- McCracken H. J. et al., 2012, *A&A*, 544, A156
- Messias H., Afonso J., Salvato M., Mobasher B., Hopkins A. M., 2012, *ApJ*, 754, 120
- Mountrichas G., Buat V., Georgantopoulos I., Yang G., Masoura V. A., Boquien M., Burgarella D., 2021, *A&A*, 653, A70
- Mullaney J. R., Alexander D. M., Goulding A. D., Hickox R. C., 2011, *MNRAS*, 414, 1082
- Murphy K. D., Yaqoob T., 2009, *MNRAS*, 397, 1549
- Nandra K. et al., 2013, preprint ([arXiv:1306.2307](https://arxiv.org/abs/1306.2307))
- Nandra K. et al., 2015, *VizieR Online Data Catalog*, J/ApJS/220/10
- Nandra K., George I. M., Mushotzky R. F., Turner T. J., Yaqoob T., 1997, *ApJ*, 477, 602
- Nandra K., O’Neill P. M., George I. M., Reeves J. N., 2007, *MNRAS*, 382, 194
- Nardini E., Risaliti G., Salvati M., Sani E., Imanishi M., Marconi A., Maiolino R., 2008, *MNRAS*, 385, L130
- Nardini E., Risaliti G., Salvati M., Sani E., Watabe Y., Marconi A., Maiolino R., 2009, *MNRAS*, 399, 1373
- O’Neill S. et al., 2022, *ApJ*, 926, L35
- Padovani P. et al., 2017, *A&AR*, 25, 2
- Park S. Q. et al., 2010, *ApJ*, 717, 1181
- Pierre M. et al., 2016, *A&A*, 592, A1
- Piro L., Yamauchi M., Matsuoka M., 1990, *ApJ*, 360, L35
- Pouliasis E., Mountrichas G., Georgantopoulos I., Ruiz A., Yang M., Bonanos A. Z., 2020, *MNRAS*, 495, 1853
- Predehl P. et al., 2021, *A&A*, 647, A1
- Press W. H., Teukolsky S. A., Vetterling W. T., Flannery B. P., 1992, *Numerical recipes in FORTRAN. The Art of Scientific Computing*, 2nd edn. Cambridge Univ. Press, Cambridge
- Ramos Almeida C. et al., 2009, *ApJ*, 702, 1127
- Ramos Almeida C., Ricci C., 2017, *Nat. Astron.*, 1, 679
- Rau A. et al., 2013, preprint ([arXiv:1308.6785](https://arxiv.org/abs/1308.6785))
- Ricci C., Ueda Y., Koss M. J., Trakhtenbrot B., Bauer F. E., Gandhi P., 2015, *ApJ*, 815, L13
- Risaliti G., Elvis M., Nicastro F., 2002, *ApJ*, 571, 234
- Risaliti G., Maiolino R., Salvati M., 1999, *ApJ*, 522, 157
- Rosario D. J., 2019, FortesFit: Flexible Spectral Energy Distribution Modelling with a Bayesian Backbone. Astrophysics Source Code Library, Michigan Technological University, preprint (ascl:1904.011)
- Saha T., Markowitz A. G., Buchner J., 2022, *MNRAS*, 509, 5485
- Salvato M. et al., 2011, *ApJ*, 742, 61
- Sanders D. B. et al., 2007, *ApJS*, 172, 86
- Scoville N. et al., 2007a, *ApJS*, 172, 1
- Scoville N. et al., 2007b, in Storrie-Lombardi L. J., Silbermann N. A., eds, *AIP Conf. Ser. Vol. 943, The Science Opportunities of the Warm Spitzer Mission Workshop*. American Institute of Physics, Melville, NY, p. 221
- Shankar F. et al., 2016, *MNRAS*, 460, 3119
- Shankar F. et al., 2020, *MNRAS*, 493, 1500
- Simmonds C., Buchner J., Salvato M., Hsu L. T., Bauer F. E., 2018, *A&A*, 618, A66
- Soltan A., 1982, *MNRAS*, 200, 115
- Stern D. et al., 2014, *ApJ*, 794, 102
- Stern D., 2015, *ApJ*, 807, 129
- Sutherland W., Saunders W., 1992, *MNRAS*, 259, 413
- Thorne J. E. et al., 2022, *MNRAS*, 509, 4940
- Treister E., Urry C. M., Virani S., 2009, *ApJ*, 696, 110
- Ueda Y., Akiyama M., Hasinger G., Miyaji T., Watson M. G., 2014, *ApJ*, 786, 104
- Ueda Y., Akiyama M., Ohta K., Miyaji T., 2003, *ApJ*, 598, 886
- Urry C. M., Padovani P., 1995, *PASP*, 107, 803
- Vito F. et al., 2018, *MNRAS*, 474, 4528
- Volonteri M., Haardt F., Madau P., 2003, *ApJ*, 582, 559
- Yang G. et al., 2017, *MNRAS*, 475, 1887

SUPPORTING INFORMATION

Supplementary data are available at *MNRAS* online.

Table 2. X-ray spectral extraction properties of the sources.

Table 6. X-ray spectral fitting results.

Please note: Oxford University Press is not responsible for the content or functionality of any supporting materials supplied by the authors.

Any queries (other than missing material) should be directed to the corresponding author for the article.

This paper has been typeset from a $\text{\TeX}/\text{\LaTeX}$ file prepared by the author.